Polarization microscopy: from ensemble structural imaging to single-molecule 3D orientation and localization microscopy

Sophie Brasselet, Miguel A Alonso

OPTICA

Polarization microscopy: from ensemble structural imaging to single-molecule 3D orientation and localization microscopy

Sophie Brasselet[1,†,*] and Miguel A. Alonso[1,2,3,†]

[1]Aix Marseille Univ, CNRS, Centrale Marseille, Institut Fresnel, F-13013 Marseille, France
[2]The Institute of Optics, University of Rochester, Rochester, New York 14627, USA
[3]miguel.alonso@fresnel.fr
[†]These authors contributed equally to this work.
*sophie.brasselet@fresnel.fr

Received 7 August 2023; revised 23 September 2023; accepted 25 September 2023; published 7 November 2023

Optical contrasts in microscopy are sensitive to light polarization, whose interaction with molecular dipoles provides an important lever for probing molecular orientation. Polarization microscopy has evolved considerably during the last decade, integrating strategies ranging from traditional linear dichroism to single-molecule orientation and localization imaging. This review aims to provide a summary of concepts and techniques behind orientation and structural imaging at the molecular level, from ensemble microscopy in 2D to single-molecule super-resolution microscopy in 3D.

https://doi.org/10.1364/OPTICA.502119

1. INTRODUCTION: PRINCIPLES OF POLARIZATION MICROSCOPY

Optical microscopy is an area of research whose steady growth has accelerated over the last few decades due to several factors: technological advances in optics, optoelectronics, laser sources, and detectors; new labeling strategies in biology; nanoscience fabrication tools in physics; and remarkable advances in computational imaging. Today optical microscopy has matured into a field in which algorithms, computing technology, and data science are of an importance comparable to that of optical design and sample optimization.

A key element in the search for improvement in optical imaging is the polarization of light. Polarization not only provides a way to obtain information on how matter is structured and organized at the molecular level but is also a degree of freedom that, along with amplitude and phase, plays a central role in structuring light. Importantly, far-field microscopy offers situations in which unconventional properties of light can be manipulated: high numerical aperture conditions and optical interfaces involve non-paraxial geometries in which longitudinal field components play an important role. It is, therefore, necessary not to rely only on the standard paraxial formalism for polarization but to consider instead a complete 3D description [1,2]. Polarized optical microscopy is a field in which fundamental and applied physics, computational sciences, and their applications in nanoscience, material science, biology, and medical sciences are still evolving and are in need of new concepts and technological advances.

An important application of polarized optics is the imaging of organization in molecular environments at the nanometric scale. Molecular interactions, which are at the core of biological phenomena and pathologies, lead to complex and heterogenous organization that is challenging to decipher, particularly in living samples. Accessing orientational organization at the molecular level is crucial for understanding key processes such as protein clustering in immunology responses, cytoskeleton filament reorganization under cell and tissue mechanical perturbations, protein aggregation in neurodegenerative diseases, and DNA organization in repair processes within the nucleus. Orientation is also a key element in biological functions at the single-molecule level. Indeed, conformational changes in proteins involve a strong reorganization of their domains at the scale of a single protein.

In this review, we aim to describe several ways in which light polarization, in particular in the non-paraxial regime, has led to important progress in imaging molecular organization. In optical microscopy, the signal depends on optical polarization via a photoselection vectorial process (excitation) and a radiation process (emission). We begin by providing an overview of the fundamentals of polarized light–matter interaction leading to such processes, both at the single-molecule and ensemble levels (Section 2). We then review advances on the two main categories of molecular organization imaging approaches: the first, mostly developed at the ensemble level, uses control of the excitation polarization of light in both fluorescence and nonlinear optical interactions (Section 3); the second, dedicated to the single-molecule level, uses control of the polarization of the fluorescence light radiated by emitters (Section 4). We focus particularly on advances in single-molecule orientation and localization microscopy (SMOLM), which is a rapidly growing field (Section 5). Section 3 and Sections 4 and

5 can be read independently. Section 6 then summarizes the properties of both excitation and emission polarized approaches, emphasizing their advantages and limitations. Finally, we discuss future challenges in the field, highlighting the possible benefits of manipulating light polarization in 3D (Section 7). Note that, while the methods addressed in this review concentrate on inverse microscopy imaging in which the molecular radiation is collected by the same objective as the illumination, transmission modalities have also been developed, some of which are mentioned in Section 3.

2. THEORETICAL BACKGROUND

The sensitivity to polarization of light–matter interaction in molecular media is due to the orientation of molecular transition dipole moments between the ground and excited states. In an incoherent process such as fluorescence, the involved molecular dipoles originate first from one-photon or multiphoton transitions in the absorption process, followed by the radiation of a de-excitation dipole in the emission process. Coherent optical processes occur instead through the radiation of induced molecular dipoles, which depend linearly (in linear scattering) or nonlinearly (in nonlinear scattering) on the incident field. In this section, we begin by giving a simplified description of the radiation of dipoles originating from molecular emitters in a microscope. We then specify the mechanisms used to excite them in both incoherent fluorescence and coherent nonlinear optical regimes.

A. Mathematical Model for the Radiation of a Dipole through a Microscope

Consider a radiating dipole with transverse coordinates $\mathbf{x} = (x, y)$, whose direction is aligned with the unit vector $\vec{\mu}$. This dipole is embedded in a medium with refractive index n_0 at a distance z_0 from the interface of this medium with a second medium with refractive index n_1, e.g., the coverslip supporting the sample, as shown in Fig. 1(a). (Note that in this article we use boldface characters for vectors with components only in the x and y directions, and characters with arrows on top for higher dimensional vectors.) As discussed later, the dipole is linked either to the direction of a fluorescent molecule or induced directly by the excitation/illumination (through a linear or nonlinear process). In both cases, the excitation of the dipole is through epi-illumination, as shown in the figure. Part of the dipole's radiation is captured by the microscope objective.

It is convenient to make the microscope telecentric, which means that the back focal plane of the objective is chosen as the pupil plane of the system, namely the location for placing an aperture stop that determines the numerical aperture (NA), because this plane is Fourier-conjugate to the object and, hence, the image. At the back focal plane, the field is essentially paraxial and is denoted as $\tilde{\mathbf{E}}(\mathbf{u})$, where $\mathbf{u} = (u\cos\varphi, u\sin\varphi)$ is a dimensionless pupil coordinate normalized so that its maximum value equals the NA of the system. If the microscope objective satisfies the Abbe sine condition and has negligible amounts of aberrations, the field at the back focal plane can be calculated through the Richards–Wolf model [3],

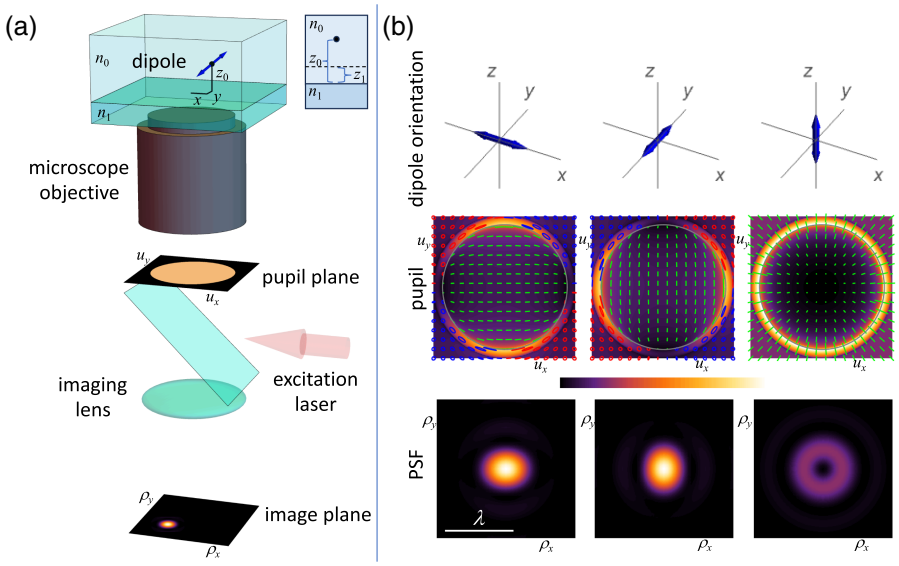

Fig. 1. (a) Principle of polarization microscopy. A dipole aligned with the unit vector $\vec{\mu}$ is generated at the coordinates (x, y, z_0) from the excitation of a molecule or particle by an incoming excitation field. The longitudinal distance z_0 is measured from the flat interface between the medium with index n_0 that embeds the dipole and another medium with index n_1. The radiation field emitted by the dipole is captured by a high numerical aperture objective lens that collimates it. A diaphragm is placed at the back focal plane (or pupil plane) to determine the numerical aperture of the system. A lens (or combination of lenses) is then used to image the dipole. The image is the result of a coherent (e.g., nonlinear optical process) or incoherent (e.g., fluorescence) summation of fields coming from all orientations explored by one dipole (e.g., single molecule imaging) or many dipoles (e.g., ensemble imaging) present within the spatial resolution of the objective and averaged in time. The dotted line in the inset at the top right represents the plane at the object space that is conjugate to the image plane, and that is at a distance z_1 from the interface. (b) First row, dipole directions aligned with the axes. Second row, the corresponding intensity and polarization distributions at the pupil plane, where the gray circle corresponds to $u = n_0$, which separates the homogeneous and evanescent components emitted by the dipole. The polarization inside the circle is always linear, and its direction is indicated by the green lines. Outside of the circle (SAF), the polarization is typically elliptical (with handedness represented in red or blue). Third row, resulting PSFs for the case NA $= n_0$ for the corresponding three dipole directions. The scale bar represents the distance that corresponds to a wavelength in the object space.

$$\tilde{\mathbf{E}}(\mathbf{u}) = A\exp\{ik[n_1 z_1 \gamma_1(\mathbf{u}) + \mathbf{u}\cdot\mathbf{x} - n_0 z_0 \gamma_0(\mathbf{u})]\}\mathbb{G}(\mathbf{u})\vec{\mu}, \quad (1)$$

where z_1 is the separation between the plane being nominally focused and the interface between the media, $\gamma_i(\mathbf{u}) = \sqrt{1-u^2/n_i^2}$, and $\mathbb{G}$ is the 2×3 Green tensor relating each component of the dipole to a field distribution in the pupil (see Supplement 1, Section 1). The second row of Fig. 1(b) shows the intensity and polarization distributions at the pupil plane for dipoles oriented along the x, y, and z directions, respectively. The gray circle corresponds to $u = n_0$. The part of the pupil outside this circle corresponds to what is known as supercritical angle fluorescence (SAF), which is the coupling of evanescent components in the medium n_0 into traveling components in the medium n_1. The figure corresponds to $z_0 \to 0$, for which SAF contributions are most important; these contributions decay exponentially with z_0.

An image is formed by performing an optical Fourier transform with a lens whose focal distance f contributes to the magnification m. The field at a detector coordinate $\boldsymbol{\rho}$ is then given by the Fourier transform,

$$\mathbf{E}(\boldsymbol{\rho}) = \frac{f}{m\lambda^2}\int \tilde{\mathbf{E}}(\mathbf{u})\exp(-ik\mathbf{u}\cdot\boldsymbol{\rho}/m)\mathrm{d}^2u = A\mathbb{K}(\mathbf{x}, z_0, z_1; \boldsymbol{\rho})\vec{\mu}, \quad (2)$$

where $\mathbb{K}$ is the 2×3 Green tensor at the image plane, given by

$$\mathbb{K}(\mathbf{x}, z_0, z_1; \boldsymbol{\rho}) = \frac{f}{m\lambda^2}\int \mathbb{G}(\mathbf{u})\exp\{ik[n_1 z_1 \gamma_1(\mathbf{u}) - n_0 z_0 \gamma_0(\mathbf{u}) + \mathbf{u}\cdot(\mathbf{x}-\boldsymbol{\rho}/m)]\}\mathrm{d}^2u. \quad (3)$$

Due to the diffraction resulting from the aperture stop, the image of the dipole $I(\boldsymbol{\rho}) = |\mathbf{E}(\boldsymbol{\rho})|^2$ is an extended spot of light referred to as the point-spread function (PSF). The third row of Fig. 1(b) shows the PSFs for dipoles oriented along the x, y, and z directions, respectively, for NA $= n_0$ so that SAF is excluded. Notice that, due to the high NA, the PSFs for transverse dipoles resemble elongated versions of the Airy pattern, while the PSF for a longitudinal dipole has a completely different shape. The shape of the PSF depends strongly on the angle between $\vec{\mu}$ and the z axis.

In polarized microscopy, a single dipole $\vec{\mu}$ can be either the emission dipole from a fluorescence process (one-photon fluorescence 1PF, two photon fluorescence 2PF) or an induced nonlinear dipole from a coherent nonlinear process (e.g., second harmonic generation). In both cases, this dipole radiates a field expressed at the pupil plane by Eq. (1). Optical contrasts are based on the measurement of the light radiated by molecular dipoles averaged in space (over the focal volume of the microscope objective) and in time (over the integration time of the detector). Let us parametrize the molecule's dipole direction as $\vec{\mu}(\Omega) = (\sin\theta\cos\phi, \sin\theta\sin\phi, \cos\theta)$, with $\Omega = (\theta, \phi)$ representing the orientation of the dipole in the frame of its angular distribution $f(\Omega)$ [Fig. 2(a)]. This distribution characterizes the explored orientations of either a single dipole or many of them, averaged in time and space, with a mean orientation lying along the direction angles denoted as (ξ, η) [Fig. 2(a)], and an angular width denoted as δ in what follows. The goal of polarized microscopy is to access both the mean direction and width/shape of this distribution.

B. Polarized Microscopy in Fluorescence

In this section, we describe the case of fluorescence, for which polarization-resolved modalities have led to a large volume of work both at the ensemble and single-molecule levels. In fluorescence imaging, fluorescent molecular labels are used as reporters of the

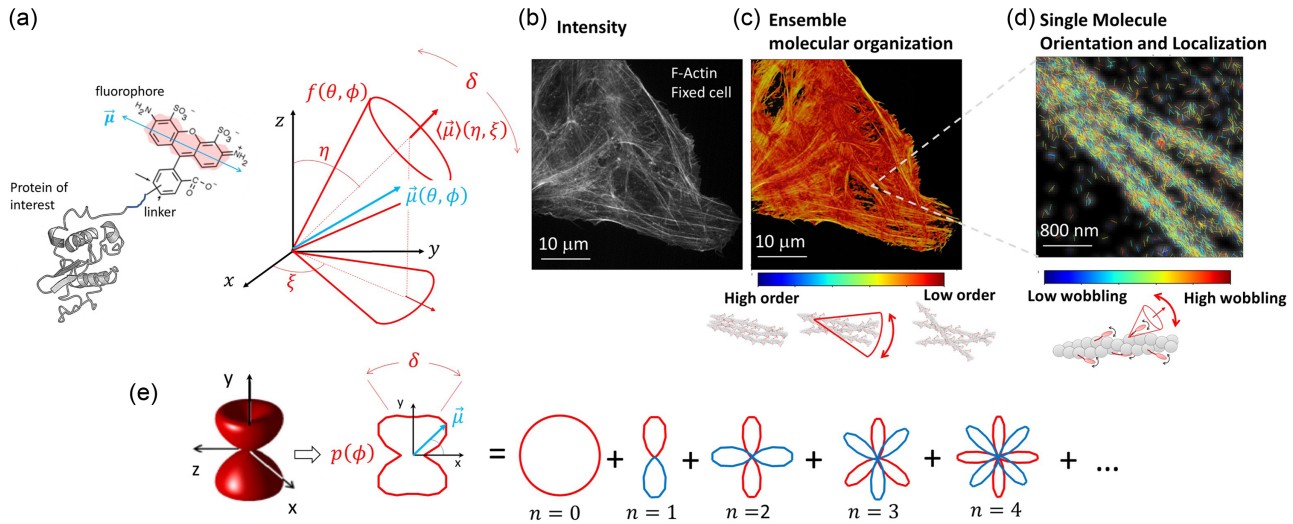

Fig. 2. (a) Schematic representation of the dipole of a fluorophore attached to a protein and definition of the angles used in this work. A single molecule or an ensemble of molecules, averaged in time and space, explore a distribution $f(\Omega)$ with $\Omega = (\theta, \phi)$ being the local orientation of the instantaneous molecular dipole in the distribution frame. The distribution, represented here as a cone, is centered at the mean direction (η, ξ), and its aperture is quantified by the cone angle δ. (b) Illustration of polarization microscopy results, showing the fluorescence intensity from emitters (here phalloidin conjugates AlexaFluor488) attached to F-actin filaments forming stress fibers in a fixed cell. (c) Ensemble molecular organization imaging, the color code representing the degree of orientation of many dipoles within the focal volume at each pixel of the image. The observed order is the result of the alignment of actin filaments, convolved with single molecule orientational fluctuations that remain despite the rigidity of the phalloidin linker to actin. (d) Single-molecule orientation and localization microscopy (SMOLM) allows the discrimination of single molecules wobbling (represented here by the color code of sticks) from their orientation (the sticks' orientation). Each stick represents a single molecule whose orientation information is added on top of its localization (adapted from [4]). (e) Schematic representation of the decomposition of the 2D projection of a molecular angular distribution into increasing symmetry orders that can be detected by different optical contrasts as described in the text.

proteins or molecules they are attached to. Figures 2(b)–2(d) illustrate polarized fluorescence imaging results obtained on a fixed cell whose F-actin filaments are labeled with a phalloidin conjugate fluorescent molecule, which is known to lie along the filaments. Polarized ensemble imaging gives an image of the molecular order, i.e., the width of $f(\Omega)$ from many molecules at each pixel location [Fig. 2(c)]. In contrast, polarized single-molecule imaging provides information on the orientation and extent of the wobbling of each molecule over time [Fig. 2(d)]. In most of the cases considered, the distribution $f(\Omega)$ is assumed to be cone-shaped with cone aperture angle δ [5,6]. Other distributions have been considered depending on the molecular labeling being used, including Gaussian-shaped [7] or "disk-shaped" distributions [8,9]. It has been shown, however, that only a limited amount of information [e.g., symmetry orders as represented in Fig. 2(e)] is accessible in polarized microscopy due to the intrinsic order of light–matter polarized interactions [10]. More details will be provided in Section 3.

Fluorescence is the result of a two-step process: absorption, which occurs with a probability density $\mathcal{P}_{\text{abs}}(\Omega_a)$ when the molecule is at an orientation Ω_a, and emission, which corresponds to the radiation efficiency of the emission dipole when the molecule is at an orientation Ω (which can be different from Ω_a, e.g., due to fast rotation) [10]. The emission efficiency depends on the fluorescence quantum yield of the molecule and the collection efficiency of the field radiated by its dipole. Since fluorescence is an optically incoherent process, the total intensity from a collection of molecules illuminated in a focal volume is the sum of the intensities radiated by their individual dipoles due to the absence of phase correlations between their respective emitted fields.

To express the fluorescence intensity as a sequential process between absorption and emission, one must account for possible orientation decorrelation between these two steps. At the scale of a fixed single molecule, these steps occur at the same orientation Ω_a, and the radiated fluorescence intensity distribution at the pupil plane is expressed as

$$I_0(\mathbf{u}) = \mathcal{P}_{\text{abs}}(\Omega_a)|\tilde{\mathbf{E}}(\mathbf{u}, \Omega_a)|^2, \tag{4}$$

where $\mathcal{P}_{\text{abs}}(\Omega)$ is the absorption probability of a dipole orientation $\vec{\mu}(\Omega)$ by an incoming field $\vec{E}^{\text{in}}$. This probability accounts for all possible excited states of the molecules, involving all transition dipole moments from the ground state to the excited states. Assuming that the molecular structure is one-dimensional (i.e., involving only one main dipole direction $\vec{\mu}(\Omega)$) [10] and that the absorption and emission transition dipoles lie along the same direction in the molecule structure (a reasonable approximation in one-dimensional fluorescent molecules), the absorption probability density can be simplified into a general form of n-photon absorption (with $n = 1$ for the most common case of one-photon fluorescence, and $n = 2$ for two-photon fluorescence),

$$\mathcal{P}_{\text{abs}}^{\text{nPF}}(\Omega_a) = |\vec{E}^{\text{in}} \cdot \vec{\mu}(\Omega_a)|^{2n}, \tag{5}$$

with $\vec{E}^{\text{in}}$ being the incident excitation field.

For molecules that possibly rotate in time, the fluorescence emission intensity is the probability of emitting a photon from the dipole orientation Ω at time t while the orientation was Ω_a at time $t = 0$, averaged over time during the long integration time of the detector. This change of orientation can occur within a time window of duration τ_f, the fluorescence lifetime, which is typically of several nanoseconds. This process depends on $g(\Omega, \Omega_a, t)$, the conditional probability density function to find a dipole along Ω after rotation from its initial position Ω_a. The distribution $g(\Omega, \Omega_a, t)$ is a solution to the rotational diffusion equation that has been described in detail within the context of constrained fluorophores [6,11]. The resulting time-averaged intensity is

$$I(\mathbf{u}) = \int \frac{1}{\tau_f} \exp\left(-\frac{t}{\tau_f}\right) \iint f(\Omega_a)\mathcal{P}_{\text{abs}}(\Omega_a) \times g(\Omega, \Omega_a, t)|\tilde{\mathbf{E}}(\mathbf{u}, \Omega)|^2 \mathrm{d}\Omega_a \mathrm{d}\Omega \mathrm{d}t. \tag{6}$$

This expression applies both in the single-molecule and ensemble contexts: a single molecule's orientation can wobble in time within the distribution $f(\Omega)$ [12], while an ensemble of molecules in the focal volume of a microscope objective can explore a distribution $f(\Omega)$ in time and space [6]. The solution to Eq. (6) has been discussed extensively [5,6,11] for molecule ensembles at the focus of a microscope objective, illustrating the benefit of polarized approaches for the study of fluorescent molecules embedded in a lipid membrane. It was later analyzed in the context of single-molecule imaging, showing that the image of rotating individual dipoles can be used as a tool to identify their orientational behavior [12].

These two situations, therefore, accept a similar description, keeping in mind that the result from an ensemble measurement is a combination of single-molecule wobbling and time-averaged organization of their ensemble. In both the ensemble and single-molecule situations, it appears that different approaches can be developed in order to decipher the way in which the molecules are organized:

- Tuning the polarization of the incident field $\vec{E}^{\text{in}}$ under unpolarized detection, in order to tune the absorption probability $P_{\text{abs}}(\Omega_a)$, giving access to the distribution $f(\Omega_a)$ of absorption dipoles. Unpolarized detection is chosen in order to extract the absorption response while ignoring the angular dependence of the emission process, $g(\Omega, \Omega_a, t)$. This technique, known as linear dichroism, is described in more detail in Section 3.B.
- Tuning the analyzed polarization in the image plane (polarization splitting) or pupil plane (by amplitude, phase, and/or polarization mask filtering) in order to probe the nature of the emitted field, $\mathbf{E}(\boldsymbol{\rho})$ or $\tilde{\mathbf{E}}(\mathbf{u})$, under isotropic or homogeneous excitation conditions. Ideally, under isotropic polarized excitation, this method allows us to probe the distribution of the emitted dipoles $f(\Omega)$. This technique, known as polarized detection, encompasses methods involving the manipulation of the polarization of the emitted field and is described in more detail in Section 5.
- Fixing both incident and emission polarizations allows the recovery of information about the rotational diffusion time of molecules, e.g., via the amount of depolarization. This approach is called fluorescence anisotropy and is most generally applied in isotropic media. It is not addressed in this review but has been widely developed in solutions [13], in microscopy [14,15], and more rarely in single-molecule imaging [16].

The retrieval of information about $f(\Omega)$ from Eq. (6) can be better visualized when considering two extreme cases: *slow* rotation (e.g., compared to the fluorescence lifetime), where the molecules do not change orientation between the absorption and emission steps, and *fast* rotation, where their rotational diffusion time is much shorter than the fluorescence lifetime. Any intermediate

scenario can be considered as a linear combination of these two limits [12].

In the slow rotation regime, the direction of the emission dipole of each single molecule is the same as that for the absorption dipole since the rotational diffusion of the molecule (with the characteristic time τ_r) is much longer than its fluorescence lifetime τ_f ($\tau_r \gg \tau_f$). The fluorescence intensity averaged over the integration time of the detector ($\tau \gg \tau_r \gg \tau_f$) can then be written as

$$I^{\text{slow}}(\mathbf{u}) = \langle \mathcal{P}_{\text{abs}}(\Omega) |\tilde{\mathbf{E}}(\mathbf{u}, \Omega)|^2 \rangle = \int \mathcal{P}_{\text{abs}}(\Omega) |\tilde{\mathbf{E}}(\mathbf{u}, \Omega)|^2 f(\Omega) \mathrm{d}\Omega, \quad (7)$$

with $\langle\rangle$ denoting an average over time and space of all molecules within the focal volume of the microscope.

In the fast rotation regime, on the other hand, the rotational diffusion is much faster than the fluorescence process ($\tau_r \ll \tau_f$), so the emission and absorption dipole directions are totally decorrelated in time, within the limits of the angular constraint of the molecular diffusion (e.g., their orientational distribution in the considered sample). This leads to a form of the fluorescence intensity in which the absorption probability and radiated fields are averaged separately. The fluorescence intensity can be written as

$$I^{\text{fast}}(\mathbf{u}) = \langle \mathcal{P}_{\text{abs}}(\Omega) \rangle \langle |\tilde{\mathbf{E}}(\mathbf{u}, \Omega)|^2 \rangle = \int \mathcal{P}_{\text{abs}}(\Omega) f(\Omega) \mathrm{d}\Omega \int |\tilde{\mathbf{E}}(\mathbf{u}, \Omega)|^2 f(\Omega) \mathrm{d}\Omega. \quad (8)$$

In Section 3, we address polarized fluorescence ensemble microscopy. Applications to single molecules and in particular localization methods for super-resolution orientation imaging are discussed in Section 5.

C. Polarized Microscopy in Coherent Nonlinear Optics

Second harmonic generation (SHG) and higher-order nonlinear processes such as third harmonic generation (THG), four wave mixing (FWM), and coherent anti-Stokes Raman scattering (CARS) are coherent processes in which $\vec{\mu}$ is a nonlinearly induced dipole. The excitation process of these optical contrasts, therefore, implies a very different readout of the orientational properties of the probed molecules: not only is the emission coherent but also there is no dependence on the rotation timescale of the molecules since the emission occurs instantaneously after excitation.

Nonlinear coherent processes have been used extensively to study biological molecules in a label-free manner, benefiting from their intrinsic nonlinear optical responses. SHG is a second-order structural contrast sensitive to non-centro-symmetric molecular organizations and has been applied to the measurement of membrane potentials thanks to SHG-active molecular lipid labels [17] or to the imaging of endogenous structural proteins such as collagen type I [18], acto-myosin, and tubulin in cells and tissues. THG is a third-order interface-sensitive contrast applied to dense structure imaging such as in lipid bodies [19]. CARS results from a third-order nonlinear interaction in resonance with molecular vibrations. It has been applied as a chemically sensitive contrast specific to biomolecular structures such as aliphatic C–H stretching vibrations in lipids [20,21]. Finally, FWM is a non-chemically specific contrast that can be applied to the visualization of molecular density, similarly as in non-resonant CARS microscopy [22].

In what follows, we illustrate the influence of light polarization on nonlinear imaging by addressing SHG, the lowest-order contrast. Similar results for higher orders can be easily derived by using the same analysis. SHG signals are generated by a linear incident field $\vec{E}^{\text{in}}$ at frequency ω. The resulting SHG intensity is the result of the coherent sum of all fields radiated at frequency 2ω by neighboring molecules within a focal volume, which are assumed to be in phase (here in the pupil plane):

$$I^{\text{SHG}}(\mathbf{u}) = |\langle \tilde{\mathrm{E}}^{\text{SHG}}(\mathbf{u}, \Omega) \rangle|^2. \quad (9)$$

In the SHG process, the single-molecule radiation field $\vec{E}^{\text{SHG}}$ originates from a nonlinearly induced dipole $\vec{\mu}^{\text{SHG}}$,

$$\mu_i^{\text{SHG}} = \sum_{j,k} \beta_{ijk}(\Omega) E_j^{\text{in}} E_k^{\text{in}}, \quad (10)$$

where $\beta_{ijk}(\Omega)$ represents the components of the second-order nonlinear susceptibility (hyperpolarizability) tensor related to the molecule active for SHG, oriented along the Euler angles $\Omega = (\theta, \phi, \psi)$ (with ψ being the rotation angle of the molecule around its own axis, which is introduced additionally since SHG is sensitive to possible molecular symmetries other than 1D [10]). Note that, in molecular systems, $\beta_{ijk}(\Omega)$ is mathematically similar to a product of three transition dipole directions whose indices are interchangeable off resonance, leading to a form similar to $\beta_{ijk}(\Omega) \propto \mu_i \mu_j \mu_k(\Omega)$ [10]. The SHG intensity results from the coherent radiation of the macroscopic dipole,

$$\mathcal{P}^{\text{SHG}} = N \int \vec{\mu}^{\text{SHG}}(\Omega) f(\Omega) \mathrm{d}\Omega = \sum_{ijk} \chi_{ijk}^{(2)} E_j^{\text{in}} E_k^{\text{in}}, \quad (11)$$

where $f(\Omega)$ is the distribution of SHG-induced dipoles within the focal volume, N is the molecular density, and $\chi^{(2)}$ is the macroscopic nonlinear second-order tensor representative of the collection of individual SHG dipoles,

$$\chi_{ijk}^{(2)} = N \int \beta_{ijk}(\Omega) f(\Omega) d\Omega. \quad (12)$$

Note that, in the paraxial approximation, the SHG intensity can be written as the modulus squared of the macroscopic SHG dipole. [A complete expression can be obtained by using Eq. (1).] The approximate SHG intensity along the polarization component i is, therefore,

$$I_i^{\text{SHG}} = \left|\mathcal{P}_i^{\text{SHG}}\right|^2 = \left| \sum_{jk} \chi_{ijk}^{(2)} E_j^{\text{in}} E_k^{\text{in}} \right|^2. \quad (13)$$

This form, which is widely used in the literature on polarized SHG [23–25], relies on two assumptions: that the illumination is homogeneous in polarization, which is valid under relatively low numerical apertures, and that the focal volume is small compared to the nonlinear coherent length, which is generally valid especially in forward detection. Several nonlinear polarized microscopy approaches are illustrated in Section 3.C, based on the principles described here.

In the following sections, we describe separately two techniques: *polarized excitation microscopy*, which consists of tuning

the excitation (i.e., incident) field $\vec{E}^{\text{in}}$ to provide information on molecule organization (Section 3), and *polarized detection microscopy*, which consists of analyzing the polarization of the radiated light (Sections 4 and 5). While the former is generally limited to the exploration of organization within a 2D projection onto the sample plane and is mostly focused on ensemble microscopy, the latter has been used for the exploration of 3D orientation organization and has been recently studied extensively in single-molecule orientation imaging.

3. POLARIZED EXCITATION MICROSCOPY: QUANTIFYING MOLECULAR ORGANIZATION IN 2D

A. Probed Organization in Ensemble Microscopy

The previous section showed that polarized excitation or detection allows us to decipher molecular organization through information about the distribution $f(\Omega)$. However, an investigation of the integrals involved in the light–matter interaction process shows that not every detail of $f(\Omega)$ is accessible [10]. In summary, the integrals involved in polarized microscopy are all in the form of n th-order moments made of the orientational average of dipoles to the nth power,

$$\int \mu_{i_1} \dots \mu_{i_n}(\Omega)\, f(\Omega) \mathrm{d}\Omega. \tag{14}$$

The order n is equal to the number of field polarizations involved in the optical process in place, encompassing both incident ($\vec{E}^{\text{in}}$) and detected ($\mathbf{E}$) fields. As $f(\Omega)$ can be decomposed into symmetry orders, this integral vanishes when these orders are of different parity than n and for orders higher than n. Decomposing $f(\Omega)$ into spherical harmonics of increasing symmetry orders provides a way to extract useful information on the quantities that can be measured from such interaction processes [10]. For $n = 2$, which occurs in one-photon fluorescence (1PF) when no polarized detection is involved, only even orders of symmetry of the distribution can be measured up to the order 2 [8]. As a result, only the mean orientation and anisotropy (i.e., the angular aperture) of a distribution can be measured, whatever its shape is. A polarized detection in 1PF would cause an increase in the accessible parameters to $n = 4$. For $n = 3$, which occurs in SHG, only odd orders can be measured, up to order 3 [26]. For $n = 4$, which occurs in 2PF/THG/CARS processes, even orders can be measured up to order 4 [27–29].

The integral in Eq. (14) and its related selection rules are at the origin of the concept of field tensor formalism, a useful picture that allows us to derive simple selection rules from light–matter interaction in high-order tensorial interactions [30,31]. Selection rules have been exploited in particular by the use of rotationally invariant field tensors, generated through the use of circular polarizations [32,33].

Both polarized fluorescence and nonlinear microscopy are based on the tuning of the incident field $\vec{E}^{\text{in}}$ to access information on the distribution $f(\Omega)$ with unpolarized detection. This is typically implemented by rotating a linear incident polarization in the plane of the sample, e.g., by using a rotating motor holding a half-wave plate, or through electro-optic modulators. An important aspect of these methods is that they restrict the accessible components to projections in the plane of the sample since this field is essentially manipulated in the sample plane. Very few examples in the literature have addressed the possibility of measuring an ensemble dipole distribution in 3D, even though methods exist that indirectly retrieve this information, exploiting both excitation and emission [34] or measuring far field scattering patterns [35]. When the incident fields are strongly focused, such as in scanning microscopy, a longitudinal polarization contribution is expected at both the excitation [3] and collection steps. This contribution can be significant when the nonlinear coupling involves axially oriented crystals [36], but it is negligible in most biological samples studied, which are generally tilted toward the sample plane [37]. For the vast majority of polarized microscopy techniques based on in-plane polarization tuning, the measured distribution is, therefore, a reduced version of $f(\Omega)$, limited to an in-plane distribution $p(\phi)$, with ϕ being the azimuthal dipole orientation in the sample plane [28,38]. A circular decomposition of this distribution allows us to identify its measurable symmetry orders [10,28,38] [Fig. 2(e)],

$$\begin{aligned} f(\Omega) = \sum_{m,J} p_m^J Y_m^J(\theta,\phi) \rightarrow p(\phi) &= \sum_n (p_n \cos n\phi + q_n \sin n\phi) \\ &= \sum_n c_n \cos n(\phi - \phi_n), \end{aligned} \tag{15}$$

with $Y_m^J(\theta,\phi)$ being the spherical harmonic of order (m, J) and p_n, q_n being the circular decomposition weights of the 2D projection of the distribution function. These orders can also be combined into a symmetry order c_n and an orientation ϕ_n. The contributions measured by different optical contrasts depend on the orders of the incident fields $\vec{E}^{\text{in}}$ involved in the processes,

$$\begin{aligned} &\text{(1PF)}\ p^{(1\text{PF})}(\phi) = p_0 + p_2 \cos 2\phi + q_2 \sin 2\phi, \\ &\text{(2PF, THG, CARS)}\ p^{(2\text{PF})}(\phi) \\ &\qquad = p_0 + p_2 \cos 2\phi + q_2 \sin 2\phi \\ &\qquad\quad + p_4 \cos 4\phi + q_4 \sin 4\phi, \\ &\text{(SHG)}\ p^{(\text{SHG})}(\phi) = p_1 \cos\phi + q_1 \sin\phi + p_3 \cos 3\phi + q_3 \sin 3\phi. \end{aligned} \tag{16}$$

In this decomposition, the lower orders $n = 1, 2$ give a quantification of the anisotropy of orientations in materials, while the higher orders 3, 4 provide a more detailed description of the shape of the distribution. Examples of the exploitation of these coupling properties for deciphering materials and biological sample properties are described in the sections that follow.

B. Linear Dichroism in Fluorescence in 2D

Linear incident light polarization interacts with fluorescent labels in a way that maximizes absorption (and thus fluorescence) when its direction lies along the fluorophore direction, defined by its absorption transition dipole moment, which is along the main conjugation direction of the label. In polarized fluorescence (called more rigorously linear dichroism), the incident field $\vec{E}^{\text{in}}$ is a linear polarization that is rotated within the sample plane at an angle α with respect to the horizontal x axis. The incident field is supposed to have a negligible longitudinal contribution and can be written as $\mathbf{E}^{\text{in}}(\alpha) \propto (\cos\alpha, \sin\alpha)$. Varying α leads to a modulation of the absorption efficiency in a molecular ensemble, $\mathcal{P}_{\text{abs}}(\alpha, \Omega) = |\mathbf{E}^{\text{in}}(\alpha) \cdot \boldsymbol{\mu}^{\text{2D}}(\phi)|^2 \sin^2\theta$, with

$\boldsymbol{\mu}^{2D}(\phi) = (\cos\phi, \sin\phi)$ being the normalized projection of the dipole onto the sample plane. In ensemble molecular imaging, the molecules are supposed to be fixed within the distribution function $f(\Omega)$ (*slow* rotation regime), and the detection is unpolarized. The contribution of the radiation field $|\tilde{\mathbf{E}}(\mathbf{u}, \Omega)|^2$ in Eq. (7) depends only on the off-plane molecular tilt angle θ. Therefore, the total fluorescence intensity, averaged over the full back focal plane, can be expressed as an α-modulated function,

$$I^{1PF} \propto \iint \mathcal{P}_{abs}(\Omega)|\vec{E}(\mathbf{u}, \Omega)|^2 f(\Omega)\mathrm{d}\Omega\mathrm{d}^2u$$

$$\propto \iint |\mathbf{E}^{in}(\alpha)\cdot\boldsymbol{\mu}^{2D}(\phi)|^2 f(\theta,\phi)J(\theta)\sin^3\theta\mathrm{d}\theta\mathrm{d}\phi, \quad (17)$$

where $J(\theta)$ is the detection probability of fluorescence, which depends on the out-of-plane dipole angle θ and the numerical aperture of the collection objective [5]. $J(\theta)$ embeds the radiation dependence of the field radiated by the emission fluorescence dipole, expressed in Eq. (1). The expression given in Eq. (17) shows that the intensity modulation $I^{1PF}(\alpha)$ depends intrinsically on a filtered part of the total distribution function $f(\Omega)$ [28],

$$p^{1PF}(\phi) = \int f(\theta,\phi)J(\theta)\sin^3\theta\mathrm{d}\theta. \quad (18)$$

The goal of polarized fluorescence imaging is to deduce the accessible orders c_n and ϕ_n of this reduced distribution function $p(\phi)$ from the $I^{1PF}(\alpha)$ dependence. Since the dipole appears at a power 2 in this expression, only the parameters $(c_2/c_0, \phi_2)$ can be retrieved. A simple way to analyze this dependence is to decompose Eq. (17) onto circular functions as

$$I^{1PF} \propto a_0 + a_2\cos 2\alpha + b_2\sin 2\alpha = I_0 + I_2\cos 2(\alpha - \Phi_2). \quad (19)$$

Only a limited number of coefficients (a_0, a_2, b_2) (or their amplitude-angle counterparts (I_0, I_2, Φ_2) with $I_0 = a_0$, $I_2 = \sqrt{a_2^2 + b_2^2}$, and $\tan\Phi_2 = b_2/a_2$) are present in this decomposition, as a result of the limited number of fields involved in the interaction process. These coefficients can be directly measured experimentally by a projection of the measured modulation onto the corresponding circular basis. The relation between the coefficients (I_2, Φ_2) and the distribution function are deduced from an analysis of Eq. (17), resulting in [28] ($I_2/I_0 = 2/3c_2/c_0$; $\tan\Phi_2 = \tan\phi_2$).

Note that the order and orientation parameters $(c_2/c_0, \phi_2)$ are directly related to the characteristics of the distribution function. Assuming that $f(\Omega)$ is a cone of aperture δ oriented along an azimuthal angle ξ with respect to the x axis [Fig. 2(a)], in the paraxial approximation where $J(\theta)$ can be ignored, these angular parameters (ξ, δ) can be easily related with $(\mathrm{sinc}\delta)^2 = (c_2/c_0)^2$; $\tan\xi = \tan\phi_2$. Other distribution shapes would lead to different dependencies. Polarized fluorescence microscopy consists of retrieving, at each pixel of an image, the order parameters (c_2/c_0) (or the distribution aperture δ) [Fig. 2(c)] and the mean orientation ξ of the distribution of molecules within the focal volume of the objective. This approach has been successfully implemented in lipids using fluorescent probes embedded in membranes, providing sensitivity to lipid phases [41] and membrane nanoscale morphological changes [8] [Fig. 3(a)].

In contrast to lipids, fluorophores attached to proteins are not necessarily attached rigidly enough to be able to report on the orientation of the protein of interest. Using polarization-sensitive fluorescence imaging to study protein organization then requires labeling protein domains in a rigid way that minimizes orientational flexibility. This has been possible *in vitro*, e.g., in protein aggregates made of amyloids fibrils [42], but also in fixed cells and tissues with phalloidin conjugates labeling of actin [39,43,44]

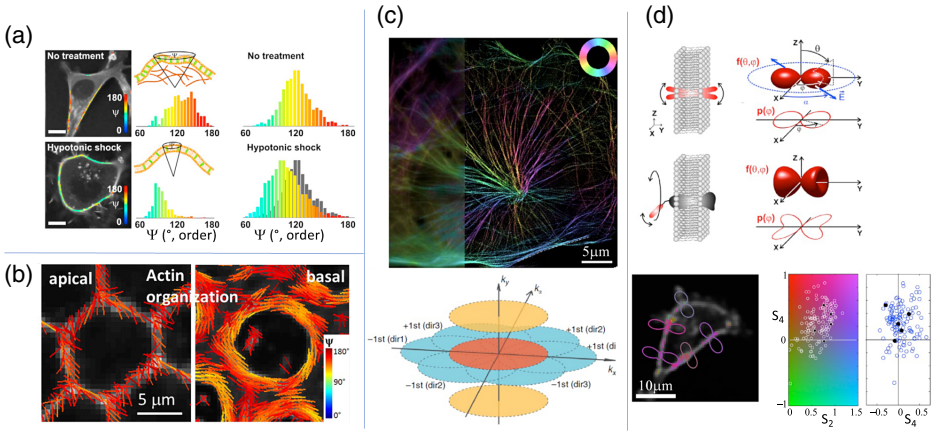

Fig. 3. 1PF/2PF polarization microscopy in 2D: linear dichroism in fluorescence. (a) Color-coded molecular order measured over a fluorescence image (gray background) in cell membranes labeled with fluorescent lipid probes. The molecular order (e.g., cone aperture of an ensemble of molecules in the focal volume) is shown to decrease when the membrane is stretched in the absence of the underlying actin cortex. (Reprinted from *Biophys. J.* **105**, A. Kress *et al.*, "Mapping the local organization of cell membranes using excitation-polarization-resolved confocal fluorescence microscopy," 127–136, Copyright 2013 with permission from Elsevier.) (b) Molecular order (stick colors) and orientation (stick orientation) shown in actin labeled with phalloidin AlexaFluor488 conjugates, in fixed drosophila embryos undergoing cellularization. At the apical surface of the cells, actin is disorganized, while at the basal membrane the presence of septin organizes actin (adapted from [39]). (c) Top, live cell imaging of microtubules in cells (labeled tubulin-GFP) using polarized standard wide field fluorescence imaging (left) and polarized structure illumination (pSIM, right). The color code corresponds to the GFP mean orientation measured at each pixel, and the pSIM image exhibits a gain in resolution. Bottom, representation of pSIM in the wave-vector space, showing the diversity of high frequency regions explored by rotating a polarized fringe pattern on the sample plane (adapted from [40]). (d) Top, examples of angular distributions probed by 2PF polarization microscopy in 2D. Bottom, illustration of the measurement of second and fourth order in distributions made of lipid probes inserted in cell membranes. (Reprinted from *Biophys. J.* **106**, A. Ferrand *et al.*, "Ultimate use of two-photon fluorescence microscopy to map orientational behavior of fluorophores," 2330–2339, Copyright 2014 with permission from Elsevier.)

[Fig. 3(b)]. Live imaging requires engineering smaller or more rigid sequences in the linker between fluorescent proteins and the protein of interest. Imaging the organization of proteins in live cells has been the object of an increasing number of strategies, such as the investigation of membrane receptor proteins [45–47], septin in yeast [48], nuclear pore complexes [49], integrin [50], and actin [51]. This approach was later applied to the determination of complex geometries in protein organization at the adhesive interface between cells, targeting the desmosomal cadherins (DCs) in cell–cell adhesion regions [52].

Recently, polarized fluorescence/linear dichroism imaging has been extended to super-resolution microscopy, using polarized structured illumination microscopy (pSIM) [40] [Fig. 3(c)] and polarized minimal photon flux (MINFLUX) microscopy [53]. The use of light polarization to also enhance spatial resolution in fluorescence imaging has been explored using sparse deconvolution of polarization-modulated fluorescent images [54], an approach that was further improved by the use of a joint reconstruction of both spatial and polarization modulation information without invoking sparsity constraints [55,56]. Finally, while polarized fluorescence imaging has mainly been developed under epi-illumination, it can also be adapted to transmission geometries [48], allowing access to thickness-averaged quantities such as birefringence and diattenuation [57], which are important readouts of molecular organization, as demonstrated in several works [58,59]. Interestingly, this geometry is applicable to other fluorescence modalities such as multi-focus microscopy (MFM) [60] and can potentially be extended to the exploration of other illumination angles such as in light-sheet microscopy.

C. Polarized Nonlinear Microscopy

The capacity of higher-order matter-optical field interactions to study fine molecular organization in materials and biological samples has been largely exploited. Nonlinear microscopy is particularly attractive for its capacity to detect molecular species without any fluorescence labeling and to access depths of several hundreds of microns in tissue by use of near-infrared illumination. A polarized nonlinear microscope is generally based on a scanning modality, in which the scan is combined with a rotation of the incident polarization, the detection being performed either in the forward or epi-direction depending on the nonlinear contrast being investigated [Fig. 4(a)]. The recorded response generally exhibits more than one harmonic in the polarization dependence due to the high order of the input fields involved [Fig. 4(a)]. Below we summarize their main properties, illustrated by important findings using these approaches.

Since they depend on the fourth power of the incident fields, both polarized 2PF (un-polarized detection) and polarized SHG give rise to a fourth-order dependence of the incident polarization angle α,

$$\begin{aligned} &I^{\mathrm{2PF,SHG}}(\alpha) \\ &= a_0 + a_2\cos 2\alpha + b_2 \sin 2\alpha + a_4 \cos 4\alpha + b_4 \sin 4\alpha \\ &= I_0 + I_2 \cos 2(\alpha - \Phi_2) + I_4 \cos 4(\alpha - \Phi_4). \end{aligned} \tag{20}$$

• In polarized 2PF, the relation between the coefficients (I_2, I_4, Φ_2, Φ_4) and the distribution function are deduced from an analysis of Eq. (20) [28] [Fig. 3(d)]. Similarly as in 1PF, following the 2D projection mechanism used in Eq. (17), 2PF polarized microscopy consists of measuring the $n = 2$, 4 orders of a projected function $p(\phi)$,

$$p^{\mathrm{2PF}}(\phi) = \int f(\theta, \phi) J(\theta) \sin^5\theta \mathrm{d}\theta. \tag{21}$$

The symmetry decomposition $p(\phi)$ is related to the intensity modulation coefficients following a direct projection, in particular ($I_2/I_0 = 2/3 c_2/c_0$) as in 1PF and ($I_4/I_0 = 1/6 c_4/c_0$). This $n = 4$ parameter allows us to obtain a higher level of detail on this distribution, particularly its sharpness, which would permit distinguishing a cone shape from a Gaussian distribution.

It has been shown that the 2PF polarized microscopy response of an ensemble of fluorescent lipid probes in artificial lipid membranes or cell membranes can report on complex organization correlated with the lipid environment [28] [Fig. 3(d)]. In particular, saturated lipid environments yield an angular distribution of fluorophores that is sharper than that of unsaturated lipids, which provide a more fluid and disordered environment. 2PF polarized microscopy has also been successfully applied to measuring the organization of membrane proteins in cell membranes [45,46].

• In polarized SHG, the involved dipoles appear to the third power (through the second-order susceptibility tensor); therefore, only odd orders of symmetry $n = 1$, 3 can be retrieved from the molecular distribution function. These orders can be related to the shape of the distribution of induced dipoles, as exploited, for instance, in collagen fibers [24,26]. Collagen polarized imaging has been a topic of great interest for decades, following the first demonstration of orientation imaging in collageneous tissue [65]. Polarized SHG monitoring in tissue has revealed the fine organization of collagen [62,66] [Fig. 4(b)] and its relation to biomedical information [64] [Fig. 4(e)], as well as mechanical properties in tissue under strain [23,67]. Polarized SHG in collagen has allowed the detection of fine effects related to aging [68] and chirality, which is measurable by nonlinear circular dichroism [69]. In collagen-rich tissues, the identification of artifacts induced by birefringence has been at the center of attention, together with solutions to correct for these effects [66,70,71]. Polarized SHG has been also applied to study nanomaterials [72–75] and interface effects in solutions, in particular water [76,77].

For higher-order nonlinear interactions, polarized contrasts involve a higher-order dependence on the input field. Third-order tensor processes in particular give rise to a sixth-order dependence of the incident polarization angle α,

$$\begin{aligned} I^{\mathrm{THG,FWM,CARS}}(\alpha) &= I_0 + I_2 \cos 2(\alpha - \Phi_2) \\ &\quad + I_4 \cos 4(\alpha - \Phi_4) + I_6 \cos 6(\alpha - \Phi_6). \end{aligned} \tag{22}$$

Because these coherent optical processes depend on susceptibility tensors of the fourth order, this polarized intensity modulation gives access to the molecular distribution function up to order 4.

• In polarized THG, the polarization sensitivity occurs essentially from the interface between two media of different refractive indices [19], which can be found mostly in lipid environments in biology. Polarized THG microscopy has allowed, in particular, quantification of the organization of lipids in tissue [61] [Fig. 4(c)]. It has also permitted us to distinguish between different types of lipid droplets in cells due to the different ordering of the two lipid species [78].

• In polarized CARS, polarization-resolved nonlinear microscopy allows the retrieval of information about the way molecular bonds are organized. Polarized CARS responses were quantified either by a direct fit of the intensity modulation [79,80] or by a projection on symmetry contributions [27]. It has been shown that accessing both second and fourth orders of the molecular distribution can bring new information on its sharpness, which could be related to lipid interactions in multilamellar lipid vesicles (MLV) of different lipid types. In particular, the cone-like nature of lipid bond distributions in MLVs could be identified in saturated lipid membranes formed by DPPC, while unsaturated lipids showed a smoother distribution [27]. This finding was later applied to polarized CARS tissue imaging, where the presence of disordered lipids was found in the lipid membranes formed by the myelin sheath around neurons in fixed mice spinal cords [63] [Fig. 4(d)].

• Combining different polarized contrasts can be valuable when exploring molecular interactions at the molecular scale. A study combining 2PF and polarized coherent Raman using CARS and its stimulated Raman scattering (SRS, the background-free counterpart of CARS) [81] has shown that it is possibe to probe the influence of the existence of fluorescent probes on the organization of neighboring lipids. In this work, 2PF directly addressed lipid fluorescent probes while CARS/SRS addressed pure lipid responses via their CH_2 vibrational stretch bonds.

Different directions have recently emerged in nonlinear polarized microscopy that show the fast pace of progress in this field. First, technological advances have led to high-speed polarization imaging, using in particular fast rotating electro-optical devices that can be synchronized with high-speed scanning [82–84]. Second, the application range of nonlinear polarized microscopy is now reaching biomedical optics interests, in particular for disease diagnosis [85–87] [Fig. 4(e)]. To make nonlinear polarized microscopy largely applicable to biological tissue research, an important element to consider is light scattering and its effect on depolarization. In this direction, formalisms including Mueller and Jones tensor descriptions are currently being developed [88], which provide robust estimates for depolarizing effects in a nonlinear Mueller formalism [89].

4. POLARIZED EMISSION MICROSCOPY: THE SECOND MOMENT MATRIX

In this section and the next, we address imaging modalities based on the way the polarization of light emitted by molecular dipoles evolves while traveling through a microscope, and how it can be manipulated in order to gain information about the molecules' orientational behavior. Since these modalities are for the most part dedicated to the study of single molecules, we start by deriving the theoretical principles used in the field of single-molecule orientation measurements. Such results can nevertheless also be used to express responses from molecule ensembles.

The fluorescence intensity from a wobbling single molecule can be expressed in a simple way following Eq. (2), assuming an isotropic excitation that eliminates the dependence on the absorption cross-section. More complex situations involving non-isotropic excitation and slow rotational motion have been taken into account indirectly [90] or introduced in more complex expressions [12,91], using similar principles as in what follows. The measured PSF is given by the directional average of the intensity at the detector over the wobbling distribution $f(\Omega)$,

$$I(\boldsymbol{\rho}) = \langle |\mathbf{E}(\boldsymbol{\rho})|^2 \rangle = A^2 \mathrm{Tr}[\mathbb{K}(\mathbf{x}, z_0, z_1; \boldsymbol{\rho}) \mathbb{M} \mathbb{K}^{\dagger}(\mathbf{x}, z_0, z_1; \boldsymbol{\rho})], \tag{23}$$

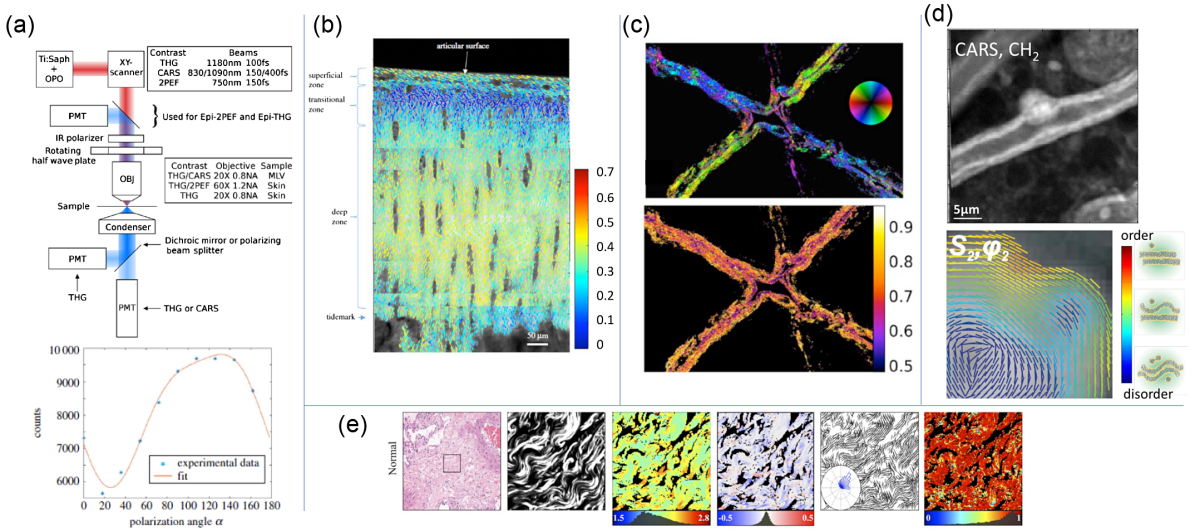

Fig. 4. Coherent nonlinear polarization microscopy. (a) General scheme of a nonlinear microscope in which polarization control of the incident beam provides a polarized contrast for SHG, 2PF, THG, and CARS (adapted from [61]). Bottom, typical response from a nonlinear polarized SHG (pSHG) signal, exhibiting the presence of several harmonics in the polarization response (adapted from [62]). (b) pSHG applied to collagen in a sagittal section of bovine articular cartilage, depicting a graduation of molecular order toward the cartilage surface in an arcade structure (adapted from [62]). (c) pTHG in human skin biopsies, evidencing lipid orientation and ordering within interfaces. A strong modulation is observed from ordered phases (adapted from [61]). (d) pCARS in lipids from the myelin sheath of fixed spinal cord mouse tissue (intensity). The zoomed region shows molecular order (color) and mean orientation (stick direction) of the lipids. (Reprinted from *Biophys. J.* **113**, A. Gasecka *et al.*, "Lipid order degradation in autoimmune demyelination probed by polarized coherent Raman microscopy," 1520–1530, Copyright 2017 with permission from Elsevier.) (e) pSHG imaging of the structural alteration of collagen in cell lung carcinoma *ex vivo* tissues, depicting different contrasts such as the degree of linear polarization (e.g., molecular order), orientation, and chiral and achiral components of the nonlinear SHG tensor (adapted from [64]).

where † denotes transpose conjugation and $\mathbb{M} = \langle \vec{\mu}\vec{\mu}^\dagger \rangle$ is the *second moment matrix* whose elements are given by the form in Eq. (14) for $n = 2$,

$$M_{ij} = \langle \mu_i \mu_j \rangle = \int f(\Omega)\mu_i \mu_j \mathrm{d}\Omega. \tag{24}$$

(Note that for fluorescence $\vec{\mu}$ is typically real.) From its definition, the second moment matrix is seen to be real, symmetric, and non-negative definite, and—due to the normalization of the directional distribution $f(\Omega)$—it has the following unit trace: $M_{xx} + M_{yy} + M_{zz} = \mathrm{Tr}\mathbb{M} = \langle \vec{\mu} \cdot \vec{\mu} \rangle = \langle 1 \rangle = 1$. This means that only five of its nine elements can be regarded as independent parameters.

Given its linear dependence on the second moment matrix, it is useful to write the PSF in Eq. (23) in terms of a basis of PSF components $\mathcal{I}_{ij}(\boldsymbol{\rho}) = \{\mathbb{K}^\dagger(\mathbf{x}, z_0, z_1; \boldsymbol{\rho})\mathbb{K}(\mathbf{x}, z_0, z_1; \boldsymbol{\rho})\}_{ij}$ as [92–94]

$$\begin{aligned} I(\boldsymbol{\rho}) &= A^2 \sum_{ij=x,y,z} M_{ij}\mathcal{I}_{ij}(\boldsymbol{\rho}) \\ &= A^2[M_{xx}\mathcal{I}_{xx}(\boldsymbol{\rho}) + M_{yy}\mathcal{I}_{yy}(\boldsymbol{\rho}) + M_{zz}\mathcal{I}_{zz}(\boldsymbol{\rho}) \\ &\quad + 2M_{xy}\mathcal{I}_{xy}(\boldsymbol{\rho}) + 2M_{xz}\mathcal{I}_{xz}(\boldsymbol{\rho}) + 2M_{yz}\mathcal{I}_{yz}(\boldsymbol{\rho})]. \end{aligned} \tag{25}$$

It is the goal of polarized emission microscopy to quantify the components of the second-order matrix of a sample. These coefficients depend entirely on the orientational behavior of the molecular dipoles, which contain both their mean 3D orientation and their second-order parameters, which relate to single-molecule wobbling/ensemble molecular order. Similarly as in ensemble 1PF polarized excitation microscopy (Section 3), the level of detail obtained on this molecular order is limited to order 2. However, here the information is no longer limited to 2D since the matrix elements that involve the longitudinal dimension are also accessible.

In what follows, we take advantage of analogies between the analysis of wobbling/disordered dipoles and that of 3D polarized fields that appear in the context of non-paraxial optics [1,2]. The relation between fluorescence and 3D polarization was recognized almost a century ago by Soleillet [95]. Theoretical formalisms that have been used for 3D polarization can prove useful in the study and development of polarized microscopy, one example being the decomposition of the matrix into an appropriate basis of Hermitian matrices. The elements of the 3×3 second-order matrix can then be slightly rearranged by using the Stokes–Gell–Mann parameters [2,94,96], which are the coefficients of the expansion of the matrix in terms of Gell–Mann matrices (much like the standard Stokes parameters for 2×2 polarization matrices are the coefficients of an expansion in terms of Pauli matrices). The Stokes–Gell–Mann parameters can be defined as

$$\begin{aligned} S_{11} &= M_{xx} - M_{yy}, \quad S_{12} = \frac{M_{xx} + M_{yy} - 2M_{zz}}{\sqrt{3}}, \\ S_{21} &= 2M_{yz}, \quad S_{22} = 2M_{xz}, \quad S_{23} = 2M_{xy}. \end{aligned} \tag{26}$$

(In the study of polarization, three more parameters are used that are proportional to the imaginary parts of the off-diagonal elements of the matrix, but these are not needed in this context given that the second moment matrix is real.) Note that S_{11} and S_{12} are linearly independent measures of the discrepancy between the three diagonal elements (whose sum is unity). The Stokes–Gell–Mann parameters can be assembled into a five-component vector $\vec{S} = (S_{11}, S_{12}, S_{21}, S_{22}, S_{23})$. It can be shown [2] that $|\vec{S}| \le 2/\sqrt{3}$, so it is convenient to renormalize the parameters as $s_{mn} = S_{mn}\sqrt{3}/2$ such that $\vec{s} = \vec{S}\sqrt{3}/2 = (s_{11}, s_{12}, s_{21}, s_{22}, s_{23})$.

We can now write an alternative version of Eq. (25), in which the measured PSF is expressed as a linear combination of PSF elements whose coefficients (except for the first) are the normalized Stokes–Gell–Mann parameters,

$$\begin{aligned} I(\boldsymbol{\rho}) = A^2[&\mathcal{I}_0(\boldsymbol{\rho}) + s_{11}\mathcal{I}_{11}(\boldsymbol{\rho}) + s_{12}\mathcal{I}_{12}(\boldsymbol{\rho}) \\ &+ s_{21}\mathcal{I}_{21}(\boldsymbol{\rho}) + s_{22}\mathcal{I}_{22}(\boldsymbol{\rho}) + s_{23}\mathcal{I}_{23}(\boldsymbol{\rho})]. \end{aligned} \tag{27}$$

Here, the first PSF element $\mathcal{I}_0(\boldsymbol{\rho}) = ||\mathbb{K}(\mathbf{x}, z_0, z_1; \boldsymbol{\rho})||^2/3$ is the only one that is guaranteed to be non-negative at all pixel positions $\boldsymbol{\rho}$; the remaining PSF elements $\mathcal{I}_{mn}(\boldsymbol{\rho})$ contain both positive and negative regions, but in a way that guarantees that $I(\boldsymbol{\rho}) \ge 0$ for all pixels if the parameters s_{mn} are within their valid ranges, explained later in this section. Several of the experimental methods described in the next section were proposed with the aim of measuring fluorophore direction and wobble. Essentially, these methods provide estimates of the second moment matrix for individual fluorophores, in addition to their spatial position. Clearly, the more different the elements $\mathcal{I}_{mn}(\boldsymbol{\rho})$ are, the better the estimation of s_{mn} (and hence $\mathbb{M}$) from the measured PSFs, leading to a better characterization of the directional behavior of the molecule [96]. Interestingly, it can be shown that the PSF basis formed from the Stokes–Gell–Mann parameters s_{mn} is, in this respect, more appropriate than that based on the direct second-order matrix elements M_{ij}, as it naturally separates the redundancy due to normalization.

The five-component vector $\vec{s}$ fully characterizes the second-order statistics of the fluorophore's direction and wobble. It is, therefore, important to understand the range of values that its components can take, that is, the shape of the region in the abstract 5D space that this vector inhabits. As mentioned earlier, this vector satisfies $|\vec{s}| \le 1$, with the equality being possible only for fixed dipoles. This serves as the basis for a measure of wobble, inspired by a measure of 3D polarization [2,97], given by

$$P = |\vec{s}| = \sqrt{s_{11}^2 + s_{12}^2 + s_{21}^2 + s_{22}^2 + s_{23}^2} \in [0, 1], \tag{28}$$

where $P = 0$ indicates full 3D depolarization of the emitted light, resulting, for example, from a dipole wobbling fully without restriction, while $P = 1$ indicates complete 3D polarization, implying the complete absence of wobble. However, the non-negative definiteness of $\mathbb{M}$ means that $\vec{s}$ is far more restricted [2,98] than what is implied by $|\vec{s}| \le 1$. The strict inequalities are given in Supplement 1, Section 2, and we simply give their geometric representation here. The first of these inequalities limits the two-component sub-vector (s_{11}, s_{12}) to an equilateral triangle inscribed in a unit disk, as shown in Fig. 5(a). Figure 5(b) shows a 3D extension of this 2D space including three half-cone sections (in different colors) that fit this triangle; a line emerging vertically from the point (s_{11}, s_{12}) intersects the three cones at three heights H_n. These heights bound each of the remaining parameters as $|s_{2n}| \le H_n$, but the actual restriction to these parameters is stronger: the sub-vector (s_{21}, s_{22}, s_{23}) can only inhabit the surface and interior of the rounded tetrahedron shown in Fig. 5(c), which is inscribed in a box whose sides [in the same colors as the cones in

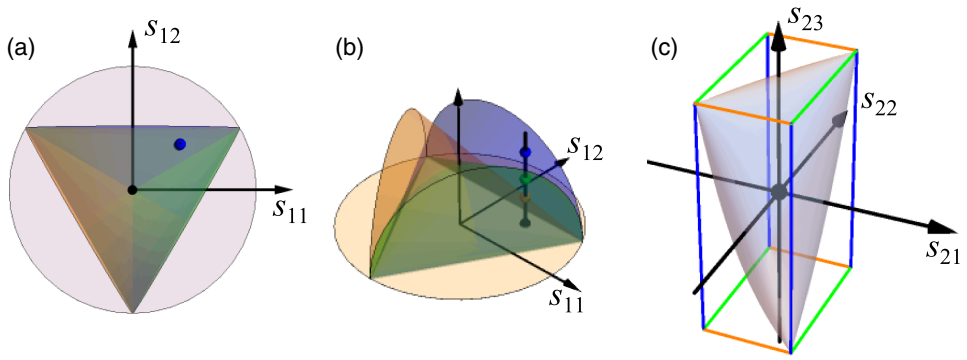

Fig. 5. Restrictions for the normalized Stokes–Gell–Mann parameters. (a) The sub-vector (s_{11}, s_{12}) is constrained to the interior and edges of an equilateral triangle centered at the origin and whose corners are at a unit distance from the origin. (b) Definition of the quantities H_n for $n = 1$ (orange), 2 (green), and 3 (blue), given by the intersections of a line emerging from (s_{11}, s_{12}) normal to this plane with three half-cones (in the colors mentioned earlier) that fit with the equilateral triangle. (c) The sub-vector (s_{21}, s_{22}, s_{23}) is constrained to the interior and surface of a rounded tetrahedron contained in a box defined by $s_{2n} \in [-H_n, H_n]$ for $n = 1, 2, 3$. The shape of this rounded tetrahedron is such that any cross-section for a fixed value of a parameter s_{2n} is an ellipse.

Fig. 5(b)] extend from $-H_n$ to $+H_n$. Together, these restrictions mean that the full 5D vector $\vec{s}$ can only inhabit a hypervolume of size $9\pi^2/160$ (rather than $8\pi^2/15$ implied by $|\vec{s}| \leq 1$). The case of no wobble ($P = 1$) corresponds to (s_{21}, s_{22}, s_{23}) being at one of the four corners of the tetrahedron in Fig. 5(c).

Another way to describe the second moment matrix [93] is in terms of its eigenvalues λ_n and eigenvectors $\vec{v}_n$ as

$$\mathbb{M} = \sum_{n=1}^{3} \lambda_n \vec{v}_n \vec{v}_n^{\mathrm{T}}, \tag{29}$$

where without loss of generality the eigenvectors $\vec{v}_m$ can be chosen as real and orthonormal. The eigenvalues λ_n are real and non-negative, and we can order them as $\lambda_1 \geq \lambda_2 \geq \lambda_3 \geq 0$. Due to the normalization of the matrix, $\lambda_1 + \lambda_2 + \lambda_3 = 1$ so that $\lambda_1 \in [1/3, 1]$. It can be shown that P defined in Eq. (28) can be written as

$$P = \sqrt{\frac{(\lambda_1 - \lambda_2)^2 + (\lambda_2 - \lambda_3)^2 + (\lambda_1 - \lambda_3)^2}{2}}, \tag{30}$$

which equals unity when only λ_1 differs from zero, in which a case $\vec{\mu} = \pm\vec{v}_1$ (the sign being irrelevant for dipole orientation). An alternative measure of wobble is the *rotational constraint* [99], defined as

$$\gamma = \lambda_1 - \frac{\lambda_2 + \lambda_3}{2}. \tag{31}$$

As mentioned earlier, it is often assumed that the dipole oscillates uniformly within a cone of angle δ centered around a main direction $\vec{v}_1 = (\sin\eta\cos\xi, \sin\eta\sin\xi, \cos\eta)$, or at least that this cone can be used to characterize the amount of wobble. This assumption implies $\lambda_2 = \lambda_3$, for which $P = \gamma = \cos^2(\delta/4)\cos(\delta/2)$. Note, however, that breaking rotational symmetry around $\vec{v}_1$ such that $\lambda_2 \neq \lambda_3$ makes the interpretation in terms of cones difficult. Geometric representations of wobble for such cases are discussed in Supplement 1, Section 3.

5. SINGLE-MOLECULE ORIENTATION AND LOCALIZATION MICROSCOPY

While ensemble polarized microscopy is very useful for obtaining insight into the way molecules are organized, the associated methods are typically limited to a 2D projection, and most importantly they report on averaged information. In fluorescence microscopy, this means that the reported quantity is the addition of two effects: the effective structural disorder and the angular fluctuations of each molecule in the ensemble. This second effect can be addressed by measuring molecules individually. We now give a description of the rapidly growing field of single-molecule localization and orientation imaging, where different strategies have been developed to exploit super-resolution single-molecule-based methods while adding information about polarization (and hence molecule orientation). Deciphering fluorescent single-molecule orientation and localization with degree- and nanometer-level precision opens the door to new research possibilities beyond the ensemble observations described in Section 3. Downscaling orientational measurements to the single-molecule level offers the possibility of accessing new information such as slow rotational diffusion behavior and conformational changes in proteins under work [100]. If used in combination with single-molecule localization microscopy (SMLM), orientational imaging leads to a new modality known as single-molecule orientation and localization microscopy (SMOLM), where structural spatial information permits visualization of the orientational organization of proteins independently from the rotational flexibility (or wobble) of their fluorescent labels since this quantity can be estimated separately for each single molecule. In this section, we describe several of the conceptual and experimental advances that have led to the development of SMOLM.

A. Single-Molecule Localization Microscopy: Spatial Localization

Given that they are telecentric and have low levels of field-dependent aberrations, optical microscopes are able to produce PSFs whose shape is approximately independent of the transverse position $\mathbf{x}$ of the molecule being imaged. The transverse localization of a molecule beyond the diffraction limit is then possible in fluorescence microscopy through the techniques [103] collectively known as SMLM, such as photoactivated localization microscopy

(PALM) [104,105], stochastic optical reconstruction microscopy (STORM) [106,107], and point accumulation in nanoscale topography (PAINT) [108]. Single fluorescing molecules have dimensions that are much smaller than the fluorescent wavelength λ, so in standard imaging techniques they can only be resolved to within scales of the order of $\lambda/2$. SMLM techniques rely on the stochastic nature of fluorescence: the final image is composed from a stack of sequential images, where for each image only a subset of the molecules fluoresce, producing PSFs that are typically sufficiently spaced as to not overlap. The (x, y) coordinates of each molecule can then be estimated with an accuracy well below the diffraction limit. Many techniques rely on the assumption that the PSF follows an Airy pattern that is symmetric and not too different from a Gaussian. The molecule's transverse position can then be estimated as the centroid of the PSF or by fitting a Gaussian through an approach known as fluorescence imaging within 1 nm accuracy (FIONA) [109]. In addition to their lateral localization, the longitudinal position (z) of single molecules is an important parameter that is challenging to measure with high precision [103] due to the relatively poor sensitivity of their PSF to defocusing. Different strategies have been developed based on interferometric pattern illumination [110], multiple plane imaging [111–113], and PSF engineering [114,115], the latter being described in more detail below.

As discussed in Section 2, the shape of a PSF depends not only on the z coordinate of the fluorescing molecule but also on its 3D orientation, and even when in focus, it can differ considerably from the standard Airy pattern. Not long after the first SMLM approaches were proposed, it was noticed that the fluorophore's lateral localization accuracy and precision can be significantly affected by its orientation, particularly when this orientation is fixed [101,116–119] [Fig. 6(a)], but also for low wobbling conditions [120–122]. Strategies of PSF manipulation such as the use of azimuthal polarization filtering have been proposed to minimize localization biases [123]. However, the dependence of the PSF's shape on the fluorophore's orientation and longitudinal position can be viewed as a feature rather than a source of error, as it might provide a means of estimating these parameters jointly with the transverse coordinate. In fact, many authors [119–126] have envisioned ways to achieve higher spatial accuracy once a single molecule's orientation is estimated.

In what follows, we describe techniques that have been proposed to enhance the dependence of the PSF on orientation and/or longitudinal position in order to better estimate these parameters for single molecules. Under the assumption of uniform wobbling within a cone, deciphering both the 3D localization and 3D orientation of single molecules requires the estimation of six parameters: three spatial (x, y, z) and three orientational (ξ, η azimuthal and elevation tilt angles, and δ wobbling extent). For anisotropic wobble, the number of parameters grows to eight.

B. Polarized Excitation (Single-Molecule Linear Dichroism)

The first measurements of single-molecule orientation were performed not by using the shape of the PSF but by using the linear dichroism inherent in the excitation of the molecules through variations in the polarization of the excitation light. This approach was not coupled at the time with single-molecule localization, but it did shed some light on the level of new information that results from considering isolated molecules as individual radiating dipoles. These dipoles were assumed to have fixed directions during the integration time of the measurements, and only the projection onto the 2D sample plane was considered [127,128]. Note that, as explained in Section 3, linear dichroism allows only the determination of two independent parameters so that 3D orientation

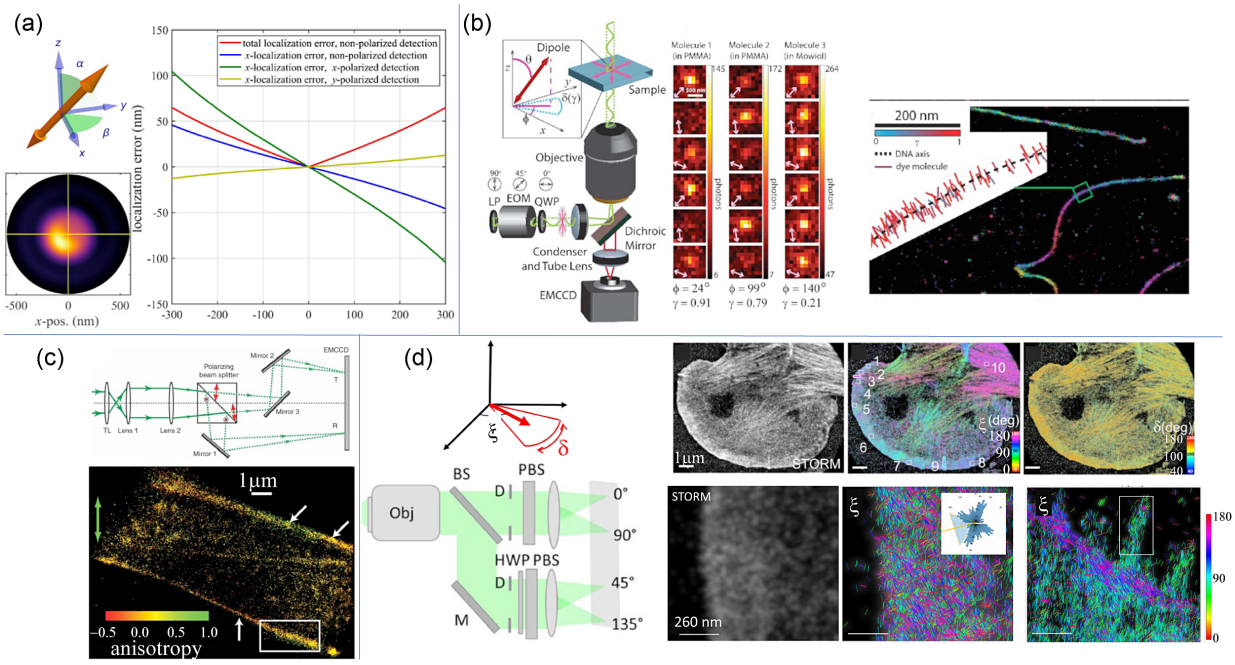

Fig. 6. (a) Bias introduced by a fixed dipole orientation on its spatial localization estimation [adapted from [101]; licensed under a Creative Commons Attribution (CC BY) license]. (b) SMOLM imaging of intercalants of DNA using excitation modulation (adapted from [102]). (c) SMOLM in isotropic media, using polarization splitting for anisotropy imaging (adapted from [16]) with permission. (d) SMOLM in organized media using a four-polarization split to retrieve both orientation and molecular order projected onto 2D. This application is illustrated in the structural imaging of actin in the dense meshwork of a cell lamellipodia (adapted from [4]).

information is not accessible except if an additional assumption is made, such as the absence of wobble. Attempts to estimate 3D orientation were performed by adding extra information, such as using multiple angles of incidence [129–133] or azimuthal illumination [134]. Although spatial localization was not used at that time, this approach led to new biological insights on DNA bending [127] and rotational mobility in lipid membranes [128] and polymers [135], as well as biological motor dynamics *in vitro* [136–140]. Single-molecule linear dichroism was later combined with 2D spatial localization by exploiting the long emission times of single emitters attached to DNA strands lying on a glass surface [102] [Fig. 6(b)].

C. Polarization Splitting

A convenient way to acquire extra information on molecular orientation without sacrificing significant numbers of photons is the one known as polarization splitting. The light emitted by a fluorophore travels through the imaging system and arrives at the detector array where it is measured. At each pixel of the detector, this light has a polarization that contains information about the fluorophore's orientation, but these detectors are typically insensitive to polarization. To capture this missing information, the light is separated into different polarization components, each of which is imaged onto a different detector or a different section of the same detector. Separation into two orthogonal linear polarizations can be easily implemented by using a polarization beamsplitter or a Nomarskii or Wollaston prism. While sufficient for many purposes, this separation into two polarization components does not allow a full polarimetric characterization; if this was required, the image can be projected onto more paths to allow more polarization projections. Similarly, a rotating analyzer can provide sequential access to polarization information. If the polarization distribution is assumed to be fairly uniform across the PSF, the separation into different polarizations allows measurement of the ratio between their intensities, which gives information about the orientation parameters, similarly to what is done in standard polarimetric techniques.

Polarized intensity estimation with no spatial localization. The first type of polarization-splitting single-molecule measurements, prior to the advent of localization microscopy, was aimed at estimating the 3D orientation of dipoles assumed to be fixed in time by using a projection onto two orthogonal linear polarizations for fluorophores specifically anchored at two ends to motor proteins [141], attached to biotin-streptavidin linkers [142], or immobilized into DNA strands [143]. This strategy was later made more precise by using total internal reflection illumination to favor longitudinal excitation and using four polarization detection channels (along the 0°, 90°, 45°, 135° directions relative to the horizontal axis of the sample) [144]. This approach was demonstrated in motors labeled with quantum rods [145] or bifunctional rhodamine molecules [146]. Polarized detection can also be achieved by a rotating analyzer [147–149], a strategy that is appropriate for non-bleaching nano-emitters [150] due to its sequential nature. The strategy of detecting multiple polarization projections was especially successful for deciphering polarization emission properties of quantum dots, in particular degenerate levels from CdSe nanocrystals [148,151,152]. Accessing information about molecule wobbling requires adding further information to polarized microscopy. If localization is ignored, this can be performed by combining both excitation and detection polarization tuning [130,139].

Polarized intensity estimation including spatial localization. Most of the early work on SMOLM consisted of combining SMLM with polarization splitting. A direct application of this approach was for fluorescence anisotropy imaging, particularly the estimation of single molecules' rotational diffusion in isotropic environments, similarly to ensemble measurements [14]. Gould *et al.* [16] obtained two-polarization split images of single-molecule anisotropy in cells, showing contrasts in membranes in particular [Fig. 6(c)]. Ohmachi *et al.* [153] used four-polarization imaging and high tilt illumination to provide both orientation and 2D spatial motion of single quantum rod-tagged myosin V proteins, assuming fixed orientations. This approach was further extended to the 3D tracking of freely moving nanoprobes [154]. Valades Cruz *et al.* [155] used a two-polarization split SMLM estimation of phalloidin conjugate single molecules attached to actin in fixed cells, providing information on their 2D structural organization under the hypothesis of homogeneous wobbling. A similar approach was used to image a single Thioflavine T molecule reporter of amyloids local structures [156]. Later, Rimoli *et al.* [4] used a four-polarization split SMLM approach to quantify the 2D projection of wobbling molecules attached to actin, providing indirect evidence of their 3D orientations [Fig. 6(d)]. Other indirect methods for the estimation of 3D orientation using a four-polarization split were applied to live actin [157] and integrin [50,158] in focal adhesion sites of live cells, using knowledge of the structure of the fluorescent construct location in the protein. Finally, a combination of polarization splitting with pupil splitting was applied recently for a complete determination of 3D orientation including wobbling, in an approach based on single-molecule intensity estimations [159,160]. The advantage of intensity estimation is that there is no need for PSF-shape fitting and that it can potentially work for compact PSFs that are more appropriate for high density SMLM imaging.

In all the work mentioned in the previous paragraph, localization is limited to 2D lateral x, y information, and since a PSF fit is not required, this estimation is based on the hypothesis of symmetric PSFs, which is valid under relatively high wobbling conditions [120]. The combination of four-polarization imaging with PSF shape fit estimation was nevertheless studied recently [161] to achieve higher precision on the estimation of the spatial and orientation parameters. This comes, however, at the cost of heavier computational work. Note also that under such geometry the estimation of the 3D orientation information and wobbling from single molecules is incomplete, as some of the PSF basis elements ($\mathcal{I}_{21}$ and $\mathcal{I}_{22}$) vanish [96].

Polarized PSF imaging. Separation into two polarization components can be particularly useful in cases where the polarization varies appreciably within the PSF, hence encoding more information. An appropriate choice of separation basis can enhance considerably the ability to estimate the 3D orientation of the fluorophore. The first approaches in this direction were designed to determine the 3D positions and 3D orientations of dipoles, without accounting for wobbling. A direct method used maximum likelihood estimation (MLE) of the shape of enlarged polarized PSFs [162], allowing separation of intra-molecular fluorescent molecules on DNA using different colors in addition to orientational information [163]. A decomposition of the PSF model onto a Hermite–Gauss basis was also implemented on four polarization projections [164]. By taking into account the proximity

of the fluorophore to a dielectric interface, wobble information was incorporated in a precise 3D orientation estimation in order to image single Nile Red molecules transiently bound to amyloid aggregates [165]. However, this method requires knowledge of the distance between the dipole and the substrate interface. As described in Section 5.E, polarization splitting is particularly effective when used in combination with PSF engineering.

D. Pupil Plane Imaging and Defocused Imaging

In parallel to polarization-splitting strategies that address mostly the image plane, a direct observation of the Fourier pupil plane can provide information on the 3D orientation of fixed dipoles [122,166], as can be appreciated from the second row in Fig. 1(b). Despite more challenging detection conditions in terms of signal-to-noise level, direct pupil plane imaging takes advantage of modifications of the emission pattern of fluorophores due to their 3D orientation [166,167] or near dielectric or metal interfaces [168,169], as described in Section 2.

An effective way to decipher a fixed single molecule's 3D orientation was later proposed based on a defocused image due to the significant difference between the longitudinal and lateral dipole radiation patterns [166,170,171]. This approach has also been widely used to analyze nanoparticles [172–175]. The analysis of defocused images in the presence of wobbling was later performed by accounting for orientational mobility in the formalism describing dipolar emission and propagation in a high numerical aperture microscope [93]. The determination of localization in addition to fixed orientations was also explored based on defocused images [92,176].

E. Point-Spread Function Engineering

The dependence of the PSF on parameters such as the orientation and longitudinal coordinate can be enhanced (or reduced) by applying a suitable filter or mask in the imaging system. In order to maintain the approximate shift invariance of the PSF to the fluorophore's transverse position, such masks must be placed at the pupil (i.e., back focal) plane. These pupil masks can modify different properties of the field distribution at the pupil, such as its amplitude, phase, or polarization. The modeling of such modified PSF uses the expressions given in Eqs. (1), (3), and (2), in which the Green matrix $\mathbb{G}(\mathbf{u})$ is multiplied by a amplitude/phase/polarization mask matrix $\mathbb{J}(\mathbf{u})$ [94]. We now describe these three different types of filtering, which of course can be combined. These methods, known as PSF engineering, were first introduced for 3D localization and were later extended for the measurement of orientation and wobble.

Amplitude filters. The amplitude distribution at the pupil plane can be modified either in a piecewise or smooth (apodized) way. The latter is less common, so we focus on the former. Amplitude filtering techniques have been proposed to measure dipole orientation based on the different distributions of optical power at the pupil plane in terms of the orientation of the fluorophore: for a dipole oriented longitudinally, a larger fraction of the power is located at the edges in comparison to a dipole contained in the transverse plane. These techniques then typically rely on splitting the wavefront before forming an image and using different sections of the pupil on each. Prior to their use for spatial localization, amplitude masks at the pupil plane were used to estimate fixed 3D dipole orientations [177]. Hohlbein [178] then used an annular mirror to separate different parts of the numerical aperture onto different paths, demonstrating high sensitivity to 3D orientations [179,180]. Pupil plane segmentation and splitting were later combined with phase masks and polarized detection to achieve complete 3D spatial localization and orientational measurements in SMOLM, as described below.

Phase filters. The most common type of mask is that of phase filters since they allow strong modifications of the PSF shape while sacrificing hardly any photons. Much work in this direction focused on either suppressing or enhancing the dependence of the PSF on the longitudinal position z of the emitter, but they have also been used to retrieve directional information, as explained in what follows:

- *Phase filters to enhance depth of focus*. An early example of a smoothly varying pupil phase mask was proposed in 1995 by Dowski and Cathy [184] to minimize the dependence of the PSF on the longitudinal coordinate, hence expanding the depth of focus of low NA imaging systems. The phase encoded by this mask has a cubic dependence in both the x and y directions, as shown in Fig. 7(a), and the 3D PSF is essentially an approximation to the Airy beam [185] (not to be confused with the Airy pattern), which is propagation invariant but traces a curved path. Other techniques have been used for enhancing the depth of focus [186]; for all of them, the image can be post-processed to alleviate the blur introduced by the mask. These techniques are not so common in SMLM since the z coordinate is an important parameter, but they have been used in light-sheet microscopy [187], where longitudinal localization is provided by the illumination.
- *Phase filters for estimatingz*. Contrary to the previous case, many phase masks are used to enhance sensitivity to z in fluorescence microscopy. Note that localization in z is possible without a phase mask since the PSF becomes wider away from defocus. There is a sign ambiguity, however, given the symmetry of the 3D PSF distribution about the nominal focal plane. This symmetry can be broken either by imaging simultaneously two slightly defocused planes [112] or by adding an amount of an appropriate aberration (the phase mask) to break the symmetry, the simplest being a splitting in the focal planes in the x and y directions through a cylindrical lens [181] [Fig. 7(b)]. More sophisticated techniques have been proposed, such as the "double helix" [115,188], which is engineered to consist of two bright spots that rotate around each other as a function of z [Fig. 7(c)], or the "tetrapod" [183,189,190] obtained through optimization of the Fisher information, which like the cylindrical lens is dominated by astigmatism but whose PSFs have more structured shapes that resemble Hermite–Gauss functions [Fig. 7(d)]. Studies with quantitative comparisons of the sensitivities of some of these techniques have been given [191].
- *Phase filters for estimating orientation, wobbling, and z*. Engineering a phase filter that allows sensitive encoding of all orientation and position parameters for single molecules is a challenge for several reasons: axial position and orientation information are difficult to discriminate in a high NA microscope; phase filtering tends to enlarge the size of a PSF to an extent that makes it incompatible with SMLM imaging in relatively dense environment; high precision estimation and accuracy are needed, even for a low photon number (typically 300–1000 photons in total over the PSF), in the presence of background (which typically ranges from 5 to 100 photons/pixel); the PSF shape must have a low sensitivity to aberrations; and computational retrieval must allow estimation of all parameters from each single molecule in a relatively short

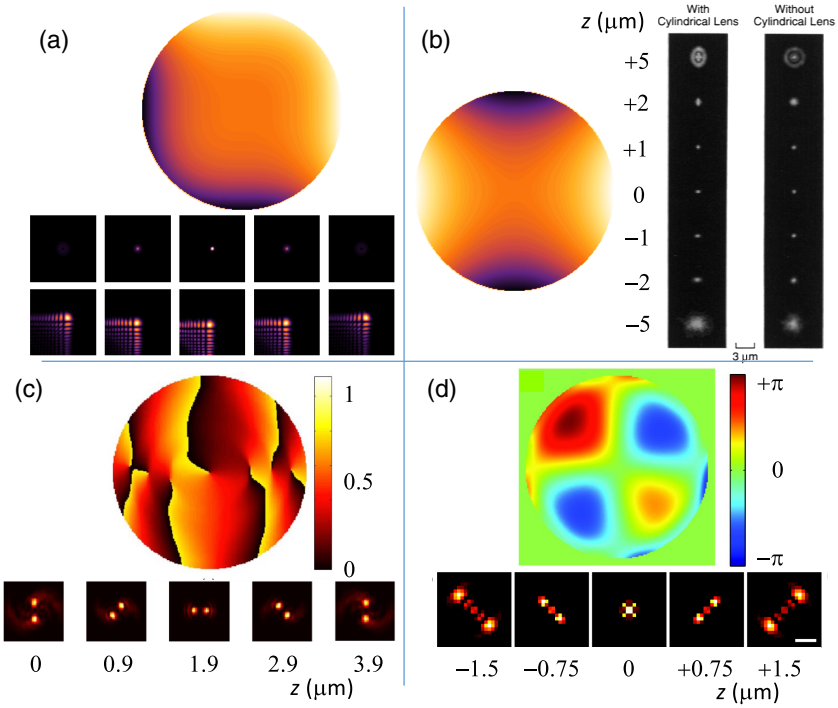

Fig. 7. Phase masks used for suppressing or enhancing PSF dependence on z. (a) Cubic phase mask (where the phase range must span many cycles, 10 in this simulation). The top row of PSFs shows for comparison the PSFs at five equally spaced distances about the focal length without the mask, while the bottom row shows those with the cubic phase masks at steps 5 times larger than for the first row. (b) Astigmatic phase resulting from using a cylindrical lens, and PSFs with an without the lens. (Reprinted from *Biophys. J.***67**, H. P. Kao and A. S. Verkman, "Tracking of single fluorescent particles in three dimensions: use of cylindrical optics to encode particle position," 1291–1300, Copyright 1994 with permission from Elsevier [181].) (c) Mask for the "double helix" PSF and corresponding PSFs at several distances (adapted from [182]). (d) Mask for the "tetrapod" PSF and corresponding PSFs at several distances. (Reprinted with permission from Y. Shechtman, S. J. Sahl, A. S. Backer, and W. E. Moerner, *Phys. Rev. Lett.***113**, 133902 (2014) [183]. Copyright 2014 by the American Physical Society. https://journals.aps.org/prl/abstract/10.1103/PhysRevLett.113.133902.)

time. The modification of the phase of dipole emission at the pupil plane to enhance sensitivity to its orientation was proposed nearly two decades ago [177,192,193], prior to the use of such strategies for localization microscopy. Different approaches have then been introduced that provide partial information about orientation (e.g., ignoring wobbling), without inferring spatial localization information. These techniques are generally combined with splitting into two linear polarization components. The simplest options consisted of applying different constant or linear phase distributions to different sections of the pupil: Foreman *et al.* used a phase step of π between two halfs of the pupil to gain sensitivity to molecule orientation [194]; Backer *et al.* separated the pupil into four quadrants and applied different linear phase ramps on each, hence separating the PSF into four points [195] such that the separation of the points gives information about longitudinal position and the relative weight of their intensities about 3D orientation; and Hashimoto *et al.* used a pupil separation in eight segments in addition to an electrically controllable polarization pattern [196]. These approaches, based on splitting the pupil plane with linear phase ramps to produce a PSF composed of several spots whose relative intensity allows orientation retrieval, are relatively robust to the presence of aberrations since no fine modification of the PSF shape itself is expected. They do tend to have, however, low signal to background ratios (SBRs) and, therefore, relatively low precision.

The complete retrieval of 3D spatial localization with 3D orientation (including wobbling), which is the core of SMOLM, requires careful design of strategies that are able to detect all parameters with high precision and with the least correlation between them. The goal of PSF engineering is to capitalize on the PSF dependence to orientation [Fig. 8(a)], emphasizing its sensitivity to angles and axial position parameters [197]. An implementation of a polarized double helix PSF has led to 3D localization and orientation estimations supposing fixed dipoles [115,120], which, however, lead to poorer estimation performances at high off-plane orientation angles and low SBRs due to a large spread of the PSF. A refinement of the quadrated pupil (the bisected pupil) [195] was proposed in which the PSF is separated into two spots with phase ramps, but in different directions for each polarization channel [198]. This approach indicated for the first time the possibility to estimate wobbling from PSF engineering [120] [Fig. 8(b)]. Zhang *et al.* proposed a version called the tri-spot phase mask, in which the pupil is separated into three sectors (with more irregular shapes), each with a linear phase ramp in a different direction to create three spots [90] [Fig. 8(c)]. The implementation of this phase mask requires the use of a spatial light modulator (SLM), and the retrieval of the parameters uses an appropriate algorithm such as maximum likelihood estimation. This work demonstrated high orientational estimation performances able to minimize 3D localization bias, which was applied to the measurement of single Atto 647 N molecules embedded in a thin layer of polymethyl methacrylate (PMMA). The tri-spot phase mask was used later to analyze the orientation behavior of Nile Red lipophilic probes transiently bound to artificial lipid membranes [199]. Finally, a phase vortex (i.e., a phase ramp in the pupil's azimuthal

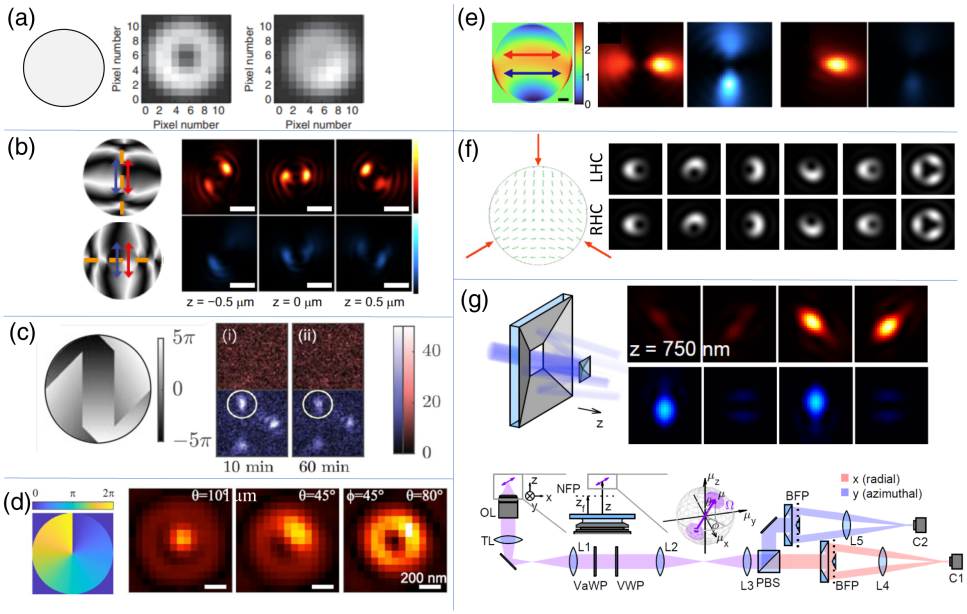

Fig. 8. SMOLM based on PSF fitting or PSF engineering. (a) Enlarged PSF from a fixed dipole (adapted from [162] with permission). (b) Bisector phase plate and PSF (adapted from [120]). (c) Tri-spot phase plate and PSF. (Reprinted with permission from O. Zhang, J. Lu, T. Ding, and M. D. Lew, *Appl. Phys. Lett.***113**, 031103 (2018) [90]. Copyright 2018 AIP Publishing LLC.) (d) Vortex phase plate and corresponding PSF (adapted from [200]). (e) Optimized phase plate and PSF (adapted from [202]). (f) CHIDO birefringent phase plate and PSF (adapted from [94]). (g) Radially and azimuthally polarized multi-view reflector and PSF (adapted from [203] with permission), with the corresponding microscope setup depicted below.

angle) was also employed, which gives a relatively compact PSF in comparison to multiple-spot phase masks [200] [Fig. 8(d)]. This strategy of direct phase imaging was modified by incorporating two orthogonally polarized detection channels [201] to enhance the sensitivity of estimation in combination with lateral x, y position estimation. This polarized vortex PSF, applied to single molecules in supported lipid layers, permitted to reach, with typically 500 photons detected, precisions of 12 nm in lateral localization and 4–8° in orientation, together with 12° wobbling angle precision. It also allowed us to estimate possible anisotropy of the directional distribution function (that is, estimating $\mathbb{M}$ even when its two lowest eigenvalues are different).

Filters with spatially varying birefringence. Another property of a nominally transparent filter that can be used for PSF engineering is birefringence. Recently, methods were proposed based on masks whose birefringence changes as a function of the pupil coordinate **u**. These techniques are used in combination with polarization splitting in order to better encode both fluorophore orientation, wobble, and longitudinal position. Curcio *et al.* [94] proposed a method called coordinate and height super-resolution imaging with dithering and orientation (CHIDO), whose filter is a glass window subjected to stress with trigonal symmetry [Fig. 8(f)]. The birefringent Fourier filter, referred to as a stress-engineered optic (SEO), naturally displays all the range of linear birefringence over the pupil, since the fast-axis orientation varies as $-\varphi/2$, and the retardance is proportional to u. Because it uses circular (rather than linear) polarization splitting, the variation in retardance has an effect similar to that of a smooth pupil splitting. CHIDO was applied to AF488 phalloidin conjugates attached to single F-actin filaments, demonstrating a tilt angle relative to the filament. In theory, this approach is able to estimate anisotropy in the wobbling. A second method [204] uses a birefringent mask corresponding to what is known as an S-plate (or a q-plate of charge 1/2), whose retardance is fixed to a half-wave, and the fast axis rotates as $\varphi/2$. This technique, called radially and azimuthally polarized (raPol) microscopy, uses linear polarization splitting and was shown to be particularly sensitive for axially oriented molecules. raPol SMOLM, which achieves 2.9 nm localization precision, 1.5° orientation precision, and 0.17 sr precision in wobbling, was applied to spherical supported lipid layers in which Nile Red fluorescent probes were inserted. Finally, Zhang *et al.* [203] developed a radially and azimuthally polarized multi-view reflector (raMVR) microscope that splits the pupil plane in addition to radial and azimuthal filtering, using a square pyramidal mirror. This approach, which provides improvement in precision at the price of increased implementation complexity [Fig. 8(g)], is based on the analysis of eight measured images.

Generation of masks. Many of the pupil masks described here have been generated with SLMs, and in theory all of them can be implemented this way. This, however, comes at the cost of photon losses by diffraction and extra complexity of the system. Photon loss can be reduced by using instead deformable mirrors [205], although the number of degrees of freedom that can be controlled is smaller. The amplitude masks are implemented with diaphragms or mirrors. Some of the phase masks can be implemented by holography or lithography [182]. Birefringent elements can now be created through several technologies such as liquid crystals, which allow for some active control. Modern nanofabrication techniques allow the fabrication of metasurfaces whose birefringence distribution can be tailored [206]. Elements like the S-plate are now commercially available. The birefringence pattern for the SEO arises naturally around an equilibrium point of a glass window under stressed-induced birefringence.

F. Optimization Criteria

Several factors must be taken into account when implementing techniques for PSF engineering. Perhaps the main one is the maximization of the information encoded. Metrics such as the Fisher information with its associated Cramér–Rao bounds [207] provide criteria for optimization, even though this is not trivial when one seeks to optimize several parameters simultaneously over a range of situations. A few recent articles reported the search for optimal phase plates in order to estimate efficiently the orientation, wobbling, and 3D positions from single molecules. One optimization strategy used the tuning of all pixels from polarized phase masks [Fig. 8(e)] [202], and deep learning approaches have also been developed [208]. While the resulting PSFs are quite large, these works show that optimization is an interesting approach through the search for efficient estimation methods.

In what follows, we summarize the important features of the use of Fisher information theory for the optimization of the efficiency of SMOLM approaches. Suppose that we have a model for the PSF intensity distribution $I(\boldsymbol{\rho};\, p)$ in terms of some source parameter p, where $\boldsymbol{\rho}$ represents the coordinates of the detector pixels. (Note that this intensity model can include some expected amount of background, not emitted by the fluorophore.) The probability that a photon will fall on a given pixel $\boldsymbol{\rho}$ is found by simply normalizing the intensity,

$$\mathcal{P}(\boldsymbol{\rho};\, p) = \frac{I(\boldsymbol{\rho};\, p)}{\langle I(\boldsymbol{\rho};\, p)\rangle_{\boldsymbol{\rho}}}, \tag{32}$$

with $\langle\cdot\rangle_{\boldsymbol{\rho}}$ denoting summation over all pixels. The Fisher information is a measure of the information carried by the PSF about the value of p. It is defined as

$$J(p) = N\left\langle \frac{[\partial_p \mathcal{P}(\boldsymbol{\rho};\, p)]^2}{\mathcal{P}(\boldsymbol{\rho};\, p)} \right\rangle_{\boldsymbol{\rho}}. \tag{33}$$

where ∂_p denotes a derivative in p and N is the number of measured photons. Therefore, as expected, the more the distribution of photons over the different pixels depends on p, the more information the measurement gives about this parameter. The Cramér–Rao bound for the variance σ_p^2 resulting from an unbiased measurement technique with an estimated result $\bar{p}$ is given by

$$\sigma_p^2 \geq 1/J(\bar{p}). \tag{34}$$

The same concepts apply to the estimation of a collection of parameters $\vec{p} = (p_1, p_2, \ldots)$. The Fisher information is now a matrix, $\mathbb{J}$, and it provides a Cramér–Rao bound for the covariance matrix $\mathbb{C}$,

$$\{\mathbb{J}(\vec{p})\}_{mn} = N\left\langle \frac{\partial_{p_m}\mathcal{P}(\boldsymbol{\rho};\, \vec{p})\partial_{p_n}\mathcal{P}(\boldsymbol{\rho};\, \vec{p})}{\mathcal{P}(\boldsymbol{\rho};\, \vec{p})} \right\rangle_{\boldsymbol{\rho}},$$

$$\vec{p}^{\,\dagger}\mathbb{C}\vec{p} \geq \vec{p}^{\,\dagger}\mathbb{J}^{-1}(\bar{\vec{p}})\vec{p}, \tag{35}$$

the inequality holding for any $\vec{p}$. A criterion for optimization of a mask is then to maximize the Fisher information of a parameter (such as longitudinal coordinate [183,189,190]) or combination of parameters (e.g., including also 3D orientation [202]) of interest over the range of values of interest. The Fisher information is also the standard approach used to compare the sensitivity of different techniques, for example, for longitudinal localization [191] and orientation [197,209,210].

Another criterion for optimization is the size of the engineered PSFs. There are two reasons for trying to achieve PSFs that are as small as possible while efficiently encoding the relevant parameters: a higher concentration of photons that improves the signal-to-noise ratio and a reduction in the occurrence of overlap of PSFs for different molecules in dense samples. The first of these criteria, however, is naturally integrated into the Fisher information if the model used to calculate it includes background [96]. Different measures for the width of a PSF exist. Some of them lend themselves to analytical minimization [211], while others must be minimized through numerical techniques.

G. Retrieving the Parameters

Several strategies can be used to retrieve the 3D positions and orientations of the fluorophores from the measured PSFs. All these approaches require a forward model able to predict the PSF position and shape for a given value of the parameters. This model can be based on theory, e.g., the one described in Section 2. However, aberrations, residual birefringence (e.g., originating from mirrors used to fold the light path) and other practical issues create discrepancies between the model and the real PSFs. In standard polarimetry techniques, these issues can be addressed by creating a model from a set of calibration measurements. This is challenging in SMOLM, however, given the nontrivial combination of the spatial (particularly the longitudinal) and directional degrees of freedom, and due to the difficulty of having controllable sources for calibration. One can use, for example, fluorescent beads [54,212–216], which combined with polarizers can mimic dipoles with given orientations, although there are inherent limitations to this approach [217]. The best option is then perhaps to use a combination of calibration measurements with theoretical calculations to arrive at a model that is complete and as close to reality as possible. Many software solutions for extracting a model from calibration measurements and for subsequently extracting 3D localization data have been proposed [205,218,219]. Some of the approaches used to retrieve the parameters from measured data are now listed.

Basis decomposition. This technique is based on the linear decomposition of the PSF in terms of a basis of elementary PSF elements, each associated with an element of the second moment matrix as in Eq. (25), or equivalently with a Stokes–Gell-Mann parameter as in Eq. (27). This approach is particularly useful for a rapid estimation of the orientation parameters for known 3D position. As mentioned earlier, the more different the basis elements are, the more accurately the parameters can be retrieved, so the goal of approaches such as polarization splitting and pupil masks is precisely to make these basis elements as large (in intensity but not in spatial extension) and as different as possible. While this approach is very simple and intuitive for the directional degrees of freedom, the mixing of the molecule's spatial coordinates makes it a bit more challenging. A method for estimating the molecule's transverse position was described in the supplementary document of [94], which also presented a way to address longitudinal localization by enlarging the basis through an expansion in z. For more accurate estimations, the results of this approach can be used as starting points for the techniques described next.

Maximum likelihood estimation. MLE [207,220] is a standard parameter retrieval technique that is optimal when the dominant noise is Poissonian and, hence, has been used in several SMOLM approaches [94,118,221,222]. The probability density $\mathcal{P}(\boldsymbol{\rho};\, \vec{p})$ can be interpreted as a measure of the *likelihood* of a given value

of the parameters $\vec{p}$ given that a photon hit pixel $\mathbf{x}$. If an experiment yields a measured PSF $\hat{I}(\boldsymbol{\rho})$ so that $\langle \hat{I}(\boldsymbol{\rho})\rangle_{\mathbf{x}} = N$, the log-likelihood distribution can be calculated as

$$\ell(\vec{p}) = \mathcal{P}_0 + \langle \hat{I}(\boldsymbol{\rho}) \log \mathcal{P}(\boldsymbol{\rho}; \vec{p})\rangle_{\boldsymbol{\rho}}, \tag{36}$$

where $\mathcal{P}_0$ is an unimportant constant. For large N, $L(\vec{p}) = \exp[\ell(\vec{p})]$ tends to a Gaussian peaked at the estimated parameter values $\bar{\vec{p}}$, and whose second moment matrix corresponds precisely to the inverse of the Fisher information matrix. The estimate for the parameters, $\bar{\vec{p}}$, then is found by maximizing $\ell(\vec{p})$.

Deep learning. Like for many other areas in science and technology, machine learning techniques such as deep learning are rapidly becoming popular. One application in SMOLM is for the retrieval of molecule parameters from large stacks of images. The two main objectives of applying this type of technique are the rapid acquisition of data and the ability to handle superposed PSFs by training the network using either simulated or experimental data. To our knowledge, the first publication in this direction appeared in 2018 for the retrieval of 2D localization [223], and by 2020, Möckl, Roy, and Moerner had already written a review of deep learning and its use by many authors in single-molecule microscopy, particularly for the retrieval of 2D and 3D localization [224]. Deep learning was subsequently applied to orientation-dependent complex PSF shapes [225] and to the joint estimation of 3D orientation and 2D localization [208,226].

6. SUMMARY

In this section, we provide a summarized comparative view of both the polarized excitation and emission microscopy approaches, addressing their main advantages and limitations as well as their applicability to a more extended range of contexts. Different factors contribute to the challenges in the development of a polarized microscopy technique, which we list in what follows.

- *Requirements in terms of labeling strategy*. As mentioned in Section 3.B, both excitation- and emission-based approaches for polarized microscopy impose a strong requirement on the type of molecules that can be observed, namely that their linker to the protein/molecule of interest should exhibit some degree of rigidity, in order to allow directional measurements. While this provides a direct, intrinsic information in label-free nonlinear microscopy, the case of fluorescence labeling is more complex since it requires that the label be attached to the protein of interest in a sufficiently rigid way. Section 3.B provides several examples of successful realizations in this respect, especially for ensemble measurements. This includes labeling for live imaging where specific constructs based on green fluorescence proteins (GFPs) have been designed for the purpose of increasing its orientational rigidity. As a general rule, long linkers such as those provided by antibodies do not provide sufficient rigidity, although several works involving single molecules have demonstrated the possibility to image biomolecular orientations via single molecule fluorescent labels, opening the way to new strategies to reduce wobbling.
- *2D versus 3D information*. While polarized emission microscopy provides today different routes to access 3D molecular orientation that can potentially be applied to both single-molecule and ensemble measurements, polarized excitation microscopy is typically limited to 2D projection, as emphasized in Section 3.B. It is possible to extend polarized excitation imaging to 3D orientations by using tilted illumination or high NA focusing in order to introduce a longitudinal excitation component. A recent study exploiting a spherical harmonic decomposition of the second-order moments in ensemble measurements also emphasized that 3D information can be accessed, provided that both excitation and emission information are exploited [34].
- *Degree of refinement of the information retrieved*. As described in Section 3.A, a strong advantage of polarized excitation imaging, especially at high orders of nonlinearity, is to provide a higher level of refinement on the molecular angular distribution function explored during the integration image time. This is visible in the higher orders of symmetry accessible in the distribution function of the molecules. In fluorescence, the combination of excitation and emission polarization control provides also a possibility to access the information on higher orders if the rotational diffusion time of the fluorescent emitter is slow with respect to its fluorescence lifetime.
- *Speed and spatial resolution*. An undeniable advantage of polarized emission imaging is its capacity to provide orientational information in a single image, while polarized excitation requires a sequential measurement for different excitation states of the incoming light. As for spatial resolution, both methods have the potential to be implemented in super-resolution microscopy, where the limit in resolution is given by both the photon budget and the imaging method being used.
- *Expansion to other imaging contexts*. Polarized excitation and emission methods can both be expanded into other optical schemes. This includes other geometries (e.g., MINFLUX, light-sheet microscopy, MFM) as mentioned in Section 3.B, as well as other optical modalities such as optical coherence tomography (OCT), scattering, or phase imaging.
- *Application to thick, scattering biological tissue*. Polarized excitation imaging is compatible with image correction schemes that have been developed to compensate for the effects of aberrations and scattering that occur in thick biological tissues. Adaptive optics and wavefront shaping tools can be developed that are sensitive to the vectorial nature of light. Polarized emission microscopy is, in contrast, potentially affected by propagation in a non-controllable way, which can be compensated for only through a preliminary characterization of the distortion. This limits the application range of polarized emission methods to thin tissue samples, cells, and membranes.

Finally, as mentioned in Section 2.B, exploiting both the excitation and emission mechanisms can open the path to new information, such as high orders of symmetry of the molecular angular distribution, or the rotational diffusion dynamics of molecules.

7. POSSIBLE FUTURE DIRECTIONS

We would like to conclude this review by listing some of the many future directions that can be explored in molecular orientation imaging. The list is by no means exhaustive, but it aims to point out some of the challenges that remain in this growing area of research and to suggest some of the strategies that could be used to tackle them, whether they be theoretical, computational, and/or experimental. Most of these challenges relate to situations in which the dimensionality of the problem is increased, either by adding degrees of freedom such as time or frequency, by considering higher-order moments of the fluorophore direction, or by

extending the treatment to cases when the radiation pattern is more complex.

A. Measurement Optimization

Many of the techniques described in this review have the aim of estimating one or several parameters of one or a group of fluorescing molecules. Some of the SMOLM methods, for example, do so by using pupil masks that are either pre-existing devices [94,200,204] or tailor-made masks designed through optimization [183,188–190,202,208]. When the goal is to measure a considerable number of degrees of freedom (e.g., three spatial coordinates and five directional parameters related to the second moment matrix for a single molecule), optimization requires defining a merit function that involves all parameters (such as the determinant of the Fisher information matrix), each within a range of interest. Even for a given combination of parameters of interest, the definition of a merit function is typically not unique: there are, for example, choices to be made on how to average this function over the range of values of interests or whether PSF compactness should be included as part of this function. Notice also that not only can the dimensionality of the measurement increase but also the number of degrees of freedom to be optimized in a measurement technique. Modern fabrication techniques allow the creation of increasingly more complex distributions of amplitude, phase, and birefringence in a mask. In cases where the optimization becomes overly complex due to the large number of parameters, deep learning techniques can be used to propose novel solutions that can at least serve as starting points for down-hill optimization routines.

B. Probing Orientational Dynamics

While polarized microscopy addresses mostly steady-state situations in which the information is averaged over time, there is a great deal of insight to be gained from time-resolved measurements. Time-resolved fluorescence anisotropy is a well-established tool for ensembles, and it is based on the measurement of the arrival time of photons that are polarized in both perpendicular and parallel directions with respect to an incoming known polarization. Using such extra information, rotational motion times shorter than the fluorescence lifetime can be accessed, providing new information on fast rotational trajectories. Time-resolved anisotropy is, however, performed mostly in isotropic environments and solutions, and it has not yet been used to address 3D rotational motion in constrained environments. It has also been developed at the single-molecule scale in fluorescence correlation spectroscopy (FCS), in which molecules diffuse freely in solution through a focus [227]. Accessing such configuration both at the ensemble and single-molecule levels is an interesting challenge, given that the current technology of time-sensitive cameras may even allow the combination of PSF engineering with time-resolved measurements. Time-resolved information could also lead to the simultaneous quantification of the rotational diffusion times of probes attached to proteins and their nanometer-scale localization, as well as to the measurement of the local viscosity or the amount of energy transfer between two nearby molecules, occurring at sub-nanometer distances.

C. Measurement of the Fourth Moment Tensor

As mentioned in Section 2.B, in the slow rotation regime in which the fluorescence lifetime is shorter than the characteristic time of molecule wobble, the excitation and detection stages are not decoupled in polarization. The measurements are, therefore, not linked to the second moment matrix $\mathbb{M}$, but to a fourth moment tensor of the form in Eq. (14) with $n = 4$. This fourth rank tensor provides more detailed information than $\mathbb{M}$ about the fluorophore's orientational dynamics and the shape of its orientational distribution, but measuring it poses interesting challenges. Unlike in the fast rotation regime where either the excitation or emission processes can be used to access the second-order moment, here both excitation and detection must work together to probe all components of the tensor. The measurement scheme will then be qualitatively similar to Mueller polarimetry, where different polarizations of the excitation field are applied, and for each the output is analyzed. This is also valid for the ensemble measurement configurations.

We can again consider techniques that are either restricted to measuring a 2D projection of the molecule orientation or that probe orientation in all three dimensions. For the 2D projection case, for which both excitation and collection can stay within the paraxial regime, the fourth moment tensor has $2^4 = 16$ elements, but by symmetry only five of them are independent, and the normalization of the direction vector $\vec{\mu}$ removes one more degree of freedom, leaving only four quantities to be measured. This number is considerably smaller than the number of elements of a Mueller matrix due to the symmetry of the tensor (and because the elements related to circular polarization are not required), so appropriate choices of polarization for the excitation and analysis can simplify the scheme. For the 3D case, on the other hand, the tensor has $3^4 = 27$ elements, which given symmetry and normalization constraints result in nine independent quantities to be measured. As discussed earlier in this article, up to five parameters related to the rotational dynamics can be extracted for a given excitation field. However, a complete measurement of the tensor will probably require more than three different excitation fields that engage in different ways all three Cartesian components of the dipole orientation. Effective techniques will then involve a cleverly chosen sequence of measurements, which will pose technological challenges associated with applying the required excitation fields, especially if this method is to be used in a super-resolution context in which both the position and directional dynamics of several fluorophores are measured simultaneously over a broad field of view.

D. Polarized Microscopy and Nanooptics: Probing Plasmonic Vector Properties, 3D Polarization States, and Complex Vector Field Structures

An interesting extension of some of the methods described in this work is to use them for probing fields rather than molecules. That is, so far we have considered that we know the excitation field and we make measurements of the radiation emitted by a molecule or collection of molecules excited by the field so that these measurements give information about these molecules. However, one can consider the situation in which we use particles whose response is well characterized to measure excitation fields. For example, the particles (e.g., metallic) can be chosen to be sufficiently small as to give a linear response in the Rayleigh scattering regime in which

the electric dipole component dominates but also to be sufficiently large as for this response to provide a sufficiently strong signal. If the 3D position of these particles is known with accuracy, they can serve as probes for measuring the unknown incident field at the particles' locations [228]. This type of approach has been used in recent years to measure a variety of different fields presenting interesting polarization features such as polarization Möbius strips [229] and transverse spin [230]. Most of these approaches have relied on using a single particle that is scanned spatially and where the measurement is performed by analyzing the field at the pupil plane. It is possible, however, to parallelize the procedure by using multiple particles while working in the image plane, using PSF engineering to best encode the information.

The measurement of local fields beyond the paraxial regime is not limited to fully deterministic fields but can also be applied to partially polarized ones. Partial polarization results from an averaging of fluctuations that is analogous to fluorophore wobble. However, unlike for the case of fluorescent dipoles, the scattered dipole emission from a nanoparticle (whether the probed field is fully or partially polarized) can include spin components, meaning that the 3×3 polarization matrix that is analogous to the second moment matrix can be complex [96]. As a result, three more Stokes–Gell–Mann parameters must be used, resulting in a polarization space composed of eight parameters [1,2]. These extra parameters should also be taken into consideration in the optimization routines used to develop appropriate measurement techniques.

E. Fluorescence from Chiral Molecules

The chirality of a molecule can result in its fluorescence being composed not only of electric dipole radiation but to also include a magnetic dipole component (and in the case of plasmonic particles, higher-order multipolar components). These different components of the radiation pattern can in theory also be resolved by a high NA microscope. In the case in which only dipolar radiation is considered, the second moment matrix must now be replaced by a 6×6 matrix that encodes both the electric and magnetic dipole components. If the electric and magnetic dipoles are assumed to be linked at all times, the number of parameters will not grow significantly, but if the directions of both types of contributions are not necessarily linked and their relative amplitudes and phases are not predetermined as a result of a known molecular structure, the space of parameters to be determined can be considerably larger. In either case, by appropriately designing a pupil mask, the PSF could in principle be engineered to encode all these parameters while still allowing localization for multiple molecules simultaneously.

Funding. Agence Nationale de la Recherche (ANR-20-CE42-0003, ANR-21-CE24-0014, France 2030 Investment Plan IDEC ANR-21-ESRE-0002, Investissements d'Avenir CENTURI ANR-16-CONV-0001, France BioImaging National Infrastructure ANR-10-INBS-04).

Acknowledgment. We thank our current and past collaborators in topics related to this work, including Luis Alemán-Castañeda, Thomas G. Brown, Valentina Curcio, Sherry Feng, Paulina Gasecka, Rodrigo Gutiérrez-Cuevas, Isael Herrera, Mathias Hofer, Naveen Kumar Balla, David Marco Castillo, Roshita Ramkhalawon, Miguel Sison, Anthony Vella, Manos Mavrakis, Patrick Ferrand, Hervé Rigneault, Julien Duboisset, and Philippe Réfrégier.

Disclosures. The authors declare that there are no conflicts of interest related to this article.

Data availability. No data were generated or analyzed in the presented research.

Supplemental document. See Supplement 1 for supporting content.

REFERENCES

1. C. Brosseau and A. Dogariu, "Symmetry properties and polarization descriptors for an arbitrary electromagnetic wavefield," Prog. Opt. **49**, 315–380 (2016).
2. M. A. Alonso, "Geometric descriptions for the polarization of nonparaxial light: a tutorial," Adv. Opt. Photon. **15**, 176–235 (2023).
3. B. Richards and E. Wolf, "Electromagnetic diffraction in optical systems. II. Structure of the image field in an aplanatic system," Proc. R. Soc. A **253**, 358–379 (1959).
4. C. V. Rimoli, C. A. Valades-Cruz, V. Curcio, M. Mavrakis, and S. Brasselet, "4polar-STORM polarized super-resolution imaging of actin filament organization in cells," Nat. Commun. **13**, 301 (2022).
5. D. Axelrod, "Carbocyanine dye orientation in red cell membrane studied by microscopic fluorescence polarization," Biophys. J. **26**, 557–573 (1979).
6. K. Florine-Casteel, "Phospholipid order in gel- and fluid-phase cell-size liposomes measured by digitized video fluorescence polarization microscopy," Biophys. J. **57**, 1199–1215 (1990).
7. C. K. Haluska, A. P. Schröder, P. Didier, D. Heissler, G. Duportail, Y. Mély, and C. M. Marques, "Combining fluorescence lifetime and polarization microscopy to discriminate phase separated domains in giant unilamellar vesicles," Biophys. J. **95**, 5737–5747 (2008).
8. A. Kress, X. Wang, H. Ranchon, J. Savatier, H. Rigneault, P. Ferrand, and S. Brasselet, "Mapping the local organization of cell membranes using excitation-polarization-resolved confocal fluorescence microscopy," Biophys. J. **105**, 127–136 (2013).
9. J. M. Brockman, A. T. Blanchard, V. Pui-Yan, W. D. Derricotte, Y. Zhang, M. E. Fay, W. A. Lam, F. A. Evangelista, A. L. Mattheyses, and K. Salaita, "Mapping the 3D orientation of piconewton integrin traction forces," Nat. Methods **15**, 115–118 (2017).
10. S. Brasselet, "Polarization-resolved nonlinear microscopy: application to structural molecular and biological imaging," Adv. Opt. Photon. **3**, 205 (2011).
11. K. Kinosita, S. Kawato, and A. Ikegami, "A theory of fluorescence polarization decay in membranes," Biophys. J. **20**, 289–305 (1977).
12. S. Stallinga, "Effect of rotational diffusion in an orientational potential well on the point spread function of electric dipole emitters," J. Opt. Soc. Am. A **32**, 213–223 (2015).
13. D. M. Jameson and J. A. Ross, "Fluorescence polarization/anisotropy in diagnostics and imaging," Chem. Rev. **110**, 2685–2708 (2010).
14. J. A. Dix and A. S. Verkman, "Mapping of fluorescence anisotropy in living cells by ratio imaging. Application to cytoplasmic viscosity," Biophys. J. **57**, 231–240 (1990).
15. A. Kress, P. Ferrand, H. Rigneault, T. Trombik, H. T. He, D. Marguet, and S. Brasselet, "Probing orientational behavior of MHC class I protein and lipid probes in cell membranes by fluorescence polarization-resolved imaging," Biophys. J. **101**, 468–476 (2011).
16. T. J. Gould, M. S. Gunewardene, M. V. Gudheti, V. V. Verkhusha, S.-R. Yin, J. A. Gosse, and S. T. Hess, "Nanoscale imaging of molecular positions and anisotropies," Nat. Methods **5**, 1027–1030 (2008).
17. L. Moreaux, V. Dambrin, M. Blanchard-Desce, J. Mertz, and T. Pons, "Electro-optic response of second-harmonic generation membrane potential sensors," Opt. Lett. **28**, 625–627 (2003).
18. A. Deniset-Besseau, J. Duboisset, E. Benichou, F. Hache, P.-F. Brevet, and M.-C. Schanne-Klein, "Measurement of the second-order hyperpolarizability of the collagen triple helix and determination of its physical origin," J. Phys. Chem. B **113**, 13437–13445 (2009).
19. D. Débarre, W. Supatto, A. M. Pena, A. Fabre, T. Tordjmann, L. Combettes, M. C. Schanne-Klein, and E. Beaurepaire, "Imaging lipid bodies in cells and tissues using third-harmonic generation microscopy," Nat. Methods **3**, 47–53 (2006).
20. A. Zumbusch, G. R. Holtom, and X. S. Xie, "Three-dimensional vibrational imaging by coherent anti-Stokes Raman scattering," Phys. Rev. Lett. **82**, 4142–4145 (1999).
21. J. X. Cheng, Y. K. Jia, G. Zheng, and X. S. Xie, "Laser-scanning coherent anti-Stokes Raman scattering microscopy and applications to cell biology," Biophys. J. **83**, 502–509 (2002).
22. D. Akimov, S. Chatzipapadopoulos, T. Meyer, N. Tarcea, B. Dietzek, M. Schmitt, and J. Popp, "Different contrast information obtained

from CARS and nonresonant FWM images," J. Raman Spectrosc. **40**, 941–947 (2009).
23. I. Gusachenko, V. Tran, Y. Houssen, J.-M. Allain, and M.-C. Schanne-Klein, "Polarization-resolved second-harmonic generation in tendon upon mechanical stretching," Biophys. J. **102**, 2220–2229 (2012).
24. K. Tilbury, C. H. Lien, S. J. Chen, and P. J. Campagnola, "Differentiation of Col I and Col III isoforms in stromal models of ovarian cancer by analysis of second harmonic generation polarization and emission directionality," Biophys. J. **106**, 354–365 (2014).
25. J.-J. Bellanger, D. Rouède, F. Tiaho, F. Ezan, and E. Schaub, "Wavy nature of collagen fibrils deduced from the dispersion of their second-order nonlinear optical anisotropy parameters," Opt. Express **28**, 4845–4858 (2020).
26. J. Duboisset, D. Aït-Belkacem, M. Roche, H. Rigneault, and S. Brasselet, "Generic model of the molecular orientational distribution probed by polarization-resolved second-harmonic generation," Phys. Rev. A **85**, 043829 (2012).
27. F.-Z. Bioud, P. Gasecka, P. Ferrand, H. Rigneault, J. Duboisset, and S. Brasselet, "Structure of molecular packing probed by polarization-resolved nonlinear four-wave mixing and coherent anti-Stokes Raman-scattering microscopy," Phys. Rev. A **89**, 013836 (2014).
28. P. Ferrand, P. Gasecka, A. Kress, X. Wang, F.-Z. Bioud, J. Duboisset, and S. Brasselet, "Ultimate use of two-photon fluorescence microscopy to map orientational behavior of fluorophores," Biophys. J. **106**, 2330–2339 (2014).
29. J. Duboisset, P. Berto, P. Gasecka, F. Z. Bioud, P. Ferrand, H. Rigneault, and S. Brasselet, "Molecular orientational order probed by coherent anti-Stokes Raman scattering (CARS) and stimulated Raman scattering (SRS) microscopy: a spectral comparative study," J. Phys. Chem. B **119**, 3242–3249 (2015).
30. B. Boulanger, J. P. Fève, and G. Marnier, "Field-factor formalism for the study of the tensorial symmetry of four-wave nonlinear optical parametric interactions in uniaxial and biaxial crystals," Phys. Rev. E **48**, 4730 (1993).
31. S. Brasselet and J. Zyss, "Relation between quantum and geometric dimensionalities in molecular nonlinear optics: beyond the two-level model for anisotropic systems," J. Nonlinear Opt. Phys. Mater. **5**, 671–693 (1996).
32. J. Duboisset, H. Rigneault, and S. Brasselet, "Filtering of matter symmetry properties by circularly polarized nonlinear optics," Phys. Rev. A **90**, 063827 (2014).
33. C. Cleff, A. Gasecka, P. Ferrand, H. Rigneault, S. Brasselet, and J. Duboisset, "Direct imaging of molecular symmetry by coherent anti-Stokes Raman scattering," Nat. Commun. **7**, 11562 (2016).
34. H. Shroff, P. L. Rivière, T. Chandler, and R. Oldenbourg, "Spatio-angular fluorescence microscopy I. Basic theory," J. Opt. Soc. Am. A **36**, 1334–1345 (2019).
35. M. Menzel, J. A. Reuter, D. Gräßel, I. Constantini, K. Amunts, and M. Axer, "Automated computation of nerve fibre inclinations from 3D polarised light imaging measurements of brain tissue," Sci. Rep. **12**, 4328 (2022).
36. C. J. R. Sheppard and E. Y. S. Yew, "Effects of axial field components on second harmonic generation microscopy," Opt. Express **14**, 1167–1174 (2006).
37. P. Schön, M. Behrndt, D. Aït-Belkacem, H. Rigneault, and S. Brasselet, "Polarization and phase pulse shaping applied to structural contrast in nonlinear microscopy imaging," Phys. Rev. A **81**, 013809 (2010).
38. P. Réfrégier, M. Roche, and S. Brasselet, "Precision analysis in polarization-resolved second harmonic generation microscopy," Opt. Lett. **36**, 2149–2151 (2011).
39. M. Mavrakis, Y. Azou-Gros, F.-C. Tsai, J. Alvarado, A. Bertin, F. Iv, A. Kress, S. Brasselet, G. Koenderink, and T. Lecuit, "Septins promote F-actin ring formation by crosslinking actin filaments into curved bundles," Nat. Cell Biol. **16**, 322–334 (2014).
40. K. Zhanghao, X. Chen, W. Liu, M. Li, Y. Liu, Y. Wang, S. Luo, X. Wang, C. Shan, H. Xie, J. Gao, X. Chen, D. Jin, X. Li, Y. Zhang, Q. Dai, and P. Xi, "Super-resolution imaging of fluorescent dipoles via polarized structured illumination microscopy," Nat. Commun. **10**, 4694 (2019).
41. R. K. Benninger, B. önfelt, M. A. Neil, D. M. Davis, and P. M. French, "Fluorescence imaging of two-photon linear dichroism: cholesterol depletion disrupts molecular orientation in cell membranes," Biophys. J. **88**, 609–622 (2005).
42. J. Duboisset, P. Ferrand, W. He, X. Wang, H. Rigneault, and S. Brasselet, "Thioflavine-T and Congo Red reveal the polymorphism of insulin amyloid fibrils when probed by polarization-resolved fluorescence microscopy," J. Phys. Chem. B **117**, 784–788 (2013).
43. M. Juanes, D. Isnardon, A. Badache, S. Brasselet, M. Mavrakis, and B. Goode, "The role of APC-mediated actin assembly in microtubule capture and focal adhesion turnover," J. Cell Biol. **218**, 3415–3435 (2019).
44. O. Loison, M. Weitkunat, A. Kaya-Çopur, C. N. Alves, T. Matzat, M. L. Spletter, S. Luschnig, S. Brasselet, P.-F. Lenne, and F. Schnorrer, "Polarization-resolved microscopy reveals a muscle myosin motor-independent mechanism of molecular actin ordering during sarcomere maturation," PLoS Biol. **16**, e2004718 (2018).
45. J. Lazar, A. Bondar, S. Timr, and S. J. Firestein, "Two-photon polarization microscopy reveals protein structure and function," Nat. Methods **8**, 684–690 (2011).
46. S. Timr, A. Bondar, L. Cwiklik, M. Štefl, M. Hof, M. Vazdar, J. Lazar, and P. Jungwirth, "Accurate determination of the orientational distribution of a fluorescent molecule in a phospholipid membrane," J. Phys. Chem. B **118**, 855–863 (2014).
47. N. Chouaki-Benmansour, K. Ruminski, A. M. Sartre, M. C. Phelipot, A. Salles, E. Bergot, A. Wu, G. Chicanne, M. Fallet, S. Brustlein, C. Billaudeau, A. Formisano, S. Mailfert, B. Payrastre, D. Marguet, S. Brasselet, Y. Hamon, and H. T. He, "Phosphoinositides regulate the TCR/CD3 complex membrane dynamics and activation," Sci. Rep. **8**, 4966 (2018).
48. B. S. Demay, N. Noda, A. S. Gladfelter, and R. Oldenbourg, "Rapid and quantitative imaging of excitation polarized fluorescence reveals ordered septin dynamics in live yeast," Biophys. J. **101**, 985–994 (2011).
49. A. L. Mattheyses, M. Kampmann, C. E. Atkinson, and S. M. Simon, "Fluorescence anisotropy reveals order and disorder of protein domains in the nuclear pore complex," Biophys. J. **99**, 1706–1717 (2010).
50. P. Nordenfelt, T. I. Moore, S. B. Mehta, J. M. Kalappurakkal, V. Swaminathan, N. Koga, T. J. Lambert, D. Baker, J. C. Waters, R. Oldenbourg, T. Tani, S. Mayor, C. M. Waterman, and T. A. Springer, "Direction of actin flow dictates integrin LFA-1 orientation during leukocyte migration," Nat. Commun. **8**, 2047 (2017).
51. A. Sugizaki, K. Sato, K. Chiba, K. Saito, M. Kawagishi, Y. Tomabechi, S. B. Mehta, H. Ishii, N. Sakai, M. Shirouzu, T. Tani, and S. Terada, "POLArIS, a versatile probe for molecular orientation, revealed actin filaments associated with microtubule asters in early embryos," Proc. Natl. Acad. Sci. USA **118**, e2019071118 (2021).
52. W. F. Dean and A. L. Mattheyses, "Defining domain-specific orientational order in the desmosomal cadherins," Biophys. J. **121**, 4325–4341 (2022).
53. Z. Zhan, C. Li, C. Li, X. Liu, X. Sun, C. He, C. Kuang, C. Kuang, C. Kuang, X. Liu, and X. Liu, "Simultaneous super-resolution estimation of single-molecule position and orientation with minimal photon fluxes," Opt. Express **30**, 22051–22065 (2022).
54. K. Zhanghao, L. Chen, X.-S. Yang, M.-Y. Wang, Z.-L. Jing, H.-B. Han, M. Q. Zhang, D. Jin, J.-T. Gao, and P. Xi, "Super-resolution dipole orientation mapping via polarization demodulation," Light Sci. Appl. **5**, e16166 (2016).
55. D. Xu, W. Zhou, J. Yin, X. Wang, and Y. Zhang, "Mapping the dipole orientation distribution within a super-resolution scale via fluorescence polarization modulation," J. Opt. Soc. Am. A **37**, 353–360 (2020).
56. M. Guan, M. Wang, K. Zhanghao, X. Zhang, M. Li, W. Liu, J. Niu, X. Yang, L. Chen, Z. Jing, M. Q. Zhang, D. Jin, P. Xi, and J. Gao, "Polarization modulation with optical lock-in detection reveals universal fluorescence anisotropy of subcellular structures in live cells," Light Sci. Appl. **11**, 4 (2022).
57. S. B. Mehta, M. Shribak, and R. Oldenbourg, "Polarized light imaging of birefringence and diattenuation at high resolution and high sensitivity," J. Opt. **15**, 094007 (2013).
58. M. McQuilken, S. B. Mehta, A. Verma, G. Harris, R. Oldenbourg, and A. S. Gladfelter, "Polarized fluorescence microscopy to study cytoskeleton assembly and organization in live cells," Curr. Protoc. Cell Biol. **67**, 4.29.1–4.29.13 (2015).
59. A. Keikhosravi, Y. Liu, C. Drifka, K. M. Woo, A. Verma, R. Oldenbourg, K. W. Eliceiri, B. Kim, J. Eichler, K. M. Reiser, A. M. Rubenchik, L. B. D. Silva, D. C. S. Tai, N. Tan, G. Xiao, H. Tang, and H. Yu, "Quantification of collagen organization in histopathology samples using liquid crystal based polarization microscopy," Biomed. Opt. Express **8**, 4243–4256 (2017).

60. C. I. Bargmann, A. S. Gladfelter, M. McQuilken, R. Heintzmann, R. Ilic, J. Larsch, S. B. Mehta, A. Verma, S. Abrahamsson, and R. Oldenbourg, "Multifocus polarization microscope (mf-polscope) for 3D polarization imaging of up to 25 focal planes simultaneously," Opt. Express **23**, 7734–7754 (2015).
61. M. Zimmerley, P. Mahou, D. Débarre, M.-C. Schanne-Klein, and E. Beaurepaire, "Probing ordered lipid assemblies with polarized third-harmonic-generation microscopy," Phys. Rev. X **3**, 011002 (2013).
62. J. C. Mansfield, V. Mandalia, A. Toms, C. P. Winlove, and S. Brasselet, "Collagen reorganization in cartilage under strain probed by polarization sensitive second harmonic generation microscopy," J. R. Soc. Interface **16**, 20180611 (2019).
63. P. Gasecka, A. Jaouen, F.-Z. Bioud, H. B. de Aguiar, J. Duboisset, P. Ferrand, H. Rigneault, N. K. Balla, F. Debarbieux, and S. Brasselet, "Lipid order degradation in autoimmune demyelination probed by polarized coherent Raman microscopy," Biophys. J. **113**, 1520–1530 (2017).
64. A. Golaraei, L. B. Mostaço-Guidolin, V. Raja, R. Navab, T. Wang, S. Sakashita, K. Yasufuku, M.-S. Tsao, B. C. Wilson, and V. Barzda, "Polarimetric second-harmonic generation microscopy of the hierarchical structure of collagen in stage I-III non-small cell lung carcinoma," Biomed. Opt. Express **11**, 1851–1863 (2020).
65. P. Stoller, K. M. Reiser, P. M. Celliers, and A. M. Rubenchik, "Polarization-modulated second harmonic generation in collagen," Biophys. J. **82**, 3330–3342 (2002).
66. I. Gusachenko, G. Latour, and M.-C. Schanne-Klein, "Polarization-resolved second harmonic microscopy in anisotropic thick tissues," Opt. Express **18**, 19339–19352 (2010).
67. D. Rouède, E. Schaub, J.-J. Bellanger, F. Ezan, J. C. Scimeca, G. Baffet, and F. Tiaho, "Determination of extracellular matrix collagen fibril architectures and pathological remodeling by polarization dependent second harmonic microscopy," Sci. Rep. **7**, 12197 (2017).
68. D. Aït-Belkacem, M. Guilbert, M. Roche, J. Duboisset, P. Ferrand, G. Sockalingum, P. Jeannesson, and S. Brasselet, "Microscopic structural study of collagen aging in isolated fibrils using polarized second harmonic generation," J. Biomed. Opt. **17**, 080506 (2012).
69. M. Schmeltz, C. Teulon, M. Pinsard, U. Hansen, M. Alnawaiseh, D. Ghoubay, V. Borderie, G. Mosser, C. Aimé, C. Aimé, F. Légaré, G. Latour, G. Latour, and M.-C. Schanne-Klein, "Circular dichroism second-harmonic generation microscopy probes the polarity distribution of collagen fibrils," Optica **7**, 1469–1476 (2020).
70. D. Ait-Belkacem, A. Gasecka, F. Munhoz, S. Brustlein, and S. Brasselet, "Influence of birefringence on polarization resolved nonlinear microscopy and collagen SHG structural imaging," Opt. Express **18**, 14859–14870 (2010).
71. I. Gusachenko and M. C. Schanne-Klein, "Numerical simulation of polarization-resolved second-harmonic microscopy in birefringent media," Phys. Rev. A **88**, 053811 (2013).
72. V. L. Floc'h, S. Brasselet, J. F. Roch, and J. Zyss, "Monitoring of orientation in molecular ensembles by polarization sensitive nonlinear microscopy," J. Phys. Chem. B **107**, 12403–12410 (2003).
73. C.-L. Hsieh, Y. Pu, R. Grange, and D. Psaltis, "Second harmonic generation from nanocrystals under linearly and circularly polarized excitations," Opt. Express **18**, 11917–11932 (2010).
74. N. K. Balla, C. Rendón-Barraza, L. M. Hoang, P. Karpinski, E. Bermúdez-Ureña, and S. Brasselet, "Polarized nonlinear nanoscopy of metal nanostructures," ACS Photon. **4**, 292–301 (2017).
75. C. Rendón-Barraza, F. Timpu, R. Grange, and S. Brasselet, "Crystalline heterogeneity in single ferroelectric nanocrystals revealed by polarized nonlinear microscopy," Sci. Rep. **9**, 1670 (2019).
76. J. Duboisset and P. F. Brevet, "Salt-induced long-to-short range orientational transition in water," Phys. Rev. Lett. **120**, 263001 (2018).
77. D. Roesel, M. Eremchev, T. Schönfeldová, S. Lee, and S. Roke, "Water as a contrast agent to quantify surface chemistry and physics using second harmonic scattering and imaging: a perspective," Appl. Phys. Lett. **120**, 160501 (2022).
78. G. Bautista, S. G. Pfisterer, M. J. Huttunen, S. Ranjan, K. Kanerva, E. Ikonen, and M. Kauranen, "Polarized THG microscopy identifies compositionally different lipid droplets in mammalian cells," Biophys. J. **107**, 2230–2236 (2014).
79. M. Zimmerley, R. Younger, T. Valenton, D. C. Oertel, J. L. Ward, and E. O. Potma, "Molecular orientation in dry and hydrated cellulose fibers: a coherent anti-Stokes Raman scattering microscopy study," J. Phys. Chem. B **114**, 10200–10208 (2010).
80. G. de Vito, A. Bifone, and V. Piazza, "Rotating-polarization cars microscopy: combining chemical and molecular orientation sensitivity," Opt. Express **20**, 29369–29377 (2012).
81. P. Gasecka, N. K. Balla, M. Sison, and S. Brasselet, "Lipids–fluorophores interactions probed by combined nonlinear polarized microscopy," J. Phys. Chem. B **125**, 13718–13729 (2021).
82. E. L. Dewalt, S. Z. Sullivan, P. D. Schmitt, R. D. Muir, and G. J. Simpson, "Polarization-modulated second harmonic generation ellipsometric microscopy at video rate," Anal. Chem. **86**, 8448–8456 (2014).
83. M. Hofer, N. K. Balla, and S. Brasselet, "High-speed polarization-resolved coherent Raman scattering imaging," Optica **4**, 795–801 (2017).
84. J. Morizet, G. Ducourthial, W. Supatto, A. Boutillon, R. Legouis, M.-C. Schanne-Klein, C. Stringari, and E. Beaurepaire, "High-speed polarization-resolved third-harmonic microscopy," Optica **6**, 385–388 (2019).
85. S. Bancelin, C. Aimé, T. Coradin, and M.-C. Schanne-Klein, "In situ three-dimensional monitoring of collagen fibrillogenesis using SHG microscopy," Biomed. Opt. Express **3**, 1446–1454 (2012).
86. R. Cisek, A. Joseph, M. Harvey, and D. Tokarz, "Polarization-sensitive second harmonic generation microscopy for investigations of diseased collagenous tissues," Front. Phys. **9**, 726996 (2021).
87. C. Raoux, C. Raoux, M. Schmeltz, M. Schmeltz, M. Bied, M. Alnawaiseh, U. Hansen, G. Latour, G. Latour, and M.-C. Schanne-Klein, "Quantitative structural imaging of keratoconic corneas using polarization-resolved SHG microscopy," Biomed. Opt. Express **12**, 4163–4178 (2021).
88. G. J. Simpson, "Connection of Jones and Mueller tensors in second harmonic generation and multi-photon fluorescence measurements," J. Phys. Chem. B **120**, 3281–3302 (2016).
89. J. R. Ulcickas and G. J. Simpson, "Mueller tensor nonlinear optical polarization analysis in turbid media," J. Phys. Chem. B **123**, 6643–6650 (2019).
90. O. Zhang, J. Lu, T. Ding, and M. D. Lew, "Imaging the three-dimensional orientation and rotational mobility of fluorescent emitters using the tri-spot point spread function," Appl. Phys. Lett. **113**, 031103 (2018).
91. E. Munger, M. Sison, and S. Brasselet, "Influence of the excitation polarization on single molecule 3D orientation imaging," Opt. Commun. **541**, 129480 (2023).
92. F. Aguet, S. G. Uhler, I. Märki, *et al.*, "Super-resolution orientation estimation and localization of fluorescent dipoles using 3-D steerable filters," Opt. Express **17**, 3125–3130 (2009).
93. A. S. Backer and W. E. Moerner, "Determining the rotational mobility of a single molecule from a single image: a numerical study," Opt. Express **23**, 4255–4276 (2015).
94. V. Curcio, L. A. Alemán-Castañeda, T. G. Brown, S. Brasselet, and M. A. Alonso, "Birefringent Fourier filtering for single molecule coordinate and height super-resolution imaging with dithering and orientation (CHIDO)," Nat. Commun. **11**, 5307 (2020).
95. P. Soleillet, "Sur les paramètres caractérisant la polarisation partielle de la lumière dans les phénomènes de fluorescence," Ann. Phys. **10**, 23–97 (1929).
96. I. Herrera, L. A. Alemán-Castañeda, S. Brasselet, and M. A. Alonso, are preparing a manuscript to be called "Stokes-based analysis for the estimation of 3D dipolar emission."
97. J. C. Samson, "Descriptions of the polarization states of vector processes: applications to ULF magnetic fields," Geophys. J. Int. **34**, 403–419 (1973).
98. F. J. Bloore, "Geometrical description of the convex sets of states for systems with spin-1/2 and spin-1," J. Phys. A **9**, 2059–2067 (1976).
99. O. Zhang and M. D. Lew, "Fundamental limits on measuring the rotational constraint of single molecules using fluorescence microscopy," Phys. Rev. Lett. **122**, 198301 (2019).
100. E. Toprak and P. R. Selvin, "New fluorescent tools for watching nanometer-scale conformational changes of single molecules," Annu. Rev. Biophys. Biomed. Struct. **36**, 349–369 (2007).
101. O. Nevskyi, R. Tsukanov, I. Gregor, N. Karedla, and J. Enderlein, "Fluorescence polarization filtering for accurate single molecule localization," APL Photon. **5**, 061302 (2020).
102. A. S. Backer, M. Y. Lee, and W. E. Moerner, "Enhanced DNA imaging using super-resolution microscopy and simultaneous single-molecule orientation measurements," Optica **3**, 659–666 (2016).

103. M. Lelek, M. T. Gyparaki, G. Beliu, F. Schueder, J. Griffié, S. Manley, R. Jungmann, M. Sauer, M. Lakadamyali, and C. Zimmer, "Single-molecule localization microscopy," Nat. Rev. Methods Primers **1**, 1–27 (2021).
104. E. Betzig, G. H. Patterson, R. Sougrat, O. W. Lindwasser, S. Olenych, J. S. Bonifacino, M. W. Davidson, J. Lippincott-Schwartz, and H. F. Hess, "Imaging intracellular fluorescent proteins at nanometer resolution," Science **313**, 1642–1645 (2006).
105. S. T. Hess, T. P. Girirajan, and M. D. Mason, "Ultra-high resolution imaging by fluorescence photoactivation localization microscopy," Biophys. J. **91**, 4258–4272 (2006).
106. M. J. Rust, M. Bates, and X. Zhuang, "Sub-diffraction-limit imaging by stochastic optical reconstruction microscopy (STORM)," Nat. Methods **3**, 793–795 (2006).
107. M. Heilemann, S. V. D. Linde, M. Schüttpelz, R. Kasper, B. Seefeldt, A. Mukherjee, P. Tinnefeld, and M. Sauer, "Subdiffraction-resolution fluorescence imaging with conventional fluorescent probes," Angew. Chem. (Int. Ed.) **47**, 6172–6176 (2008).
108. A. Sharonov and R. M. Hochstrasser, "Wide-field subdiffraction imaging by accumulated binding of diffusing probes," Proc. Natl. Acad. Sci. USA **103**, 18911–18916 (2006).
109. A. Yildiz and P. R. Selvin, "Fluorescence imaging with one nanometer accuracy, application to molecular motors," Acc. Chem. Res. **38**, 574–582 (2005).
110. G. Shtengel, J. A. Galbraith, C. G. Galbraith, J. Lippincott-Schwartz, J. M. Gillette, S. Manley, R. Sougrat, C. M. Waterman, P. Kanchanawong, M. W. Davidson, R. D. Fetter, and H. F. Hess, "Interferometric fluorescent super-resolution microscopy resolves 3D cellular ultrastructure," Proc. Natl. Acad. Sci. USA **106**, 3125–3130 (2009).
111. M. F. Juette, T. J. Gould, M. D. Lessard, M. J. Mlodzianoski, B. S. Nagpure, B. T. Bennett, S. T. Hess, and J. Bewersdorf, "Three-dimensional sub–100 nm resolution fluorescence microscopy of thick samples," Nat. Methods **5**, 527–529 (2008).
112. S. Ram, E. S. W. J. Chao, P. Prabhat, and R. Ober, "A novel approach to determining the three-dimensional location of microscopic objects with applications to 3D particle tracking," Proc. SPIE **6443**, 64430C (2007).
113. S. Abrahamsson, J. Chen, B. Hajj, S. Stallinga, A. Y. Katsov, J. Wisniewski, G. Mizuguchi, P. Soule, F. Mueller, C. D. Darzacq, X. Darzacq, C. Wu, C. I. Bargmann, D. A. Agard, M. Dahan, and M. G. Gustafsson, "Fast multicolor 3D imaging using aberration-corrected multifocus microscopy," Nat. Methods **10**, 60–63 (2013).
114. B. Huang, W. Wang, M. Bates, and X. Zhuang, "Three-dimensional super-resolution imaging by stochastic optical reconstruction microscopy," Science **319**, 810–813 (2008).
115. S. R. P. Pavani, M. A. Thompson, J. S. Biteen, S. J. Lord, N. Liu, R. J. Twieg, R. Piestun, and W. E. Moerner, "Three-dimensional, single-molecule fluorescence imaging beyond the diffraction limit by using a double-helix point spread function," Proc. Natl. Acad. Sci. USA **106**, 2995–2999 (2009).
116. A. P. Bartko and R. M. Dickson, "Imaging three-dimensional single molecule orientations," J. Phys. Chem. B **103**, 11237–11241 (1999).
117. J. Enderlein, E. Toprak, and P. R. Selvin, "Polarization effect on position accuracy of fluorophore localization," Opt. Express **14**, 8111–8120 (2006).
118. S. Stallinga, B. Rieger, E. Betzig, G. H. Patterson, R. Sougrat, O. W. Lindwasser, S. Olenych, J. S. Bonifacino, M. W. Davidson, J. Lippincott-Schwartz, H. F. Hess, M. Heilemann, S. van de Linde, M. Schttpelz, R. Kasper, B. Seefeldt, A. Mukherjee, P. Tinnefeld, and M. Sauer, "Accuracy of the Gaussian point spread function model in 2D localization microscopy," Opt. Express **18**, 24461–24476 (2010).
119. J. Engelhardt, J. Keller, P. Hoyer, M. Reuss, T. Staudt, and S. W. Hell, "Molecular orientation affects localization accuracy in superresolution far-field fluorescence microscopy," Nano Lett. **11**, 209–213 (2011).
120. M. P. Backlund, M. D. Lew, A. S. Backer, S. J. Sahl, G. Grover, A. Agrawal, R. Piestun, and W. E. Moerner, "Simultaneous, accurate measurement of the 3D position and orientation of single molecules," Proc. Natl. Acad. Sci. USA **109**, 19087–19092 (2012).
121. M. D. Lew, M. P. Backlund, and W. E. Moerner, "Rotational mobility of single molecules affects localization accuracy in super-resolution fluorescence microscopy," Nano Lett. **13**, 3967–3972 (2013).
122. M. P. Backlund, M. D. Lew, A. S. Backer, S. J. Sahl, and W. E. Moerner, "The role of molecular dipole orientation in single-molecule fluorescence microscopy and implications for super-resolution imaging," ChemPhysChem **15**, 587–599 (2014).
123. M. D. Lew and W. E. Moerner, "Azimuthal polarization filtering for accurate, precise, and robust single-molecule localization microscopy," Nano Lett. **14**, 6407–6413 (2014).
124. S. R. P. Pavani, J. G. DeLuca, R. Piestun, E. Betzig, G. H. Patterson, R. Sougrat, O. W. Lindwasser, S. Olenych, J. S. Bonifacino, M. W. Davidson, J. Lippincott-Schwartz, and H. F. Hess, "Polarization sensitive, three-dimensional, single-molecule imaging of cells with a double-helix system," Opt. Express **17**, 19644–19655 (2009).
125. M. P. Backlund, A. Arbabi, P. N. Petrov, E. Arbabi, S. Saurabh, A. Faraon, and W. E. Moerner, "Removing orientation-induced localization biases in single-molecule microscopy using a broadband metasurface mask," Nat. Photonics **10**, 459–462 (2016).
126. F. Hinterer, M. C. Schneider, S. Hubmer, M. López-Martinez, P. Zelger, A. Jesacher, R. Ramlau, and G. J. Schütz, "Robust and bias-free localization of individual fixed dipole emitters achieving the Cramér Rao bound for applications in cryo-single molecule localization microscopy," PLoS ONE **17**, e0263500 (2022).
127. T. Ha, T. Enderle, D. S. Chemla, P. R. Selvin, and S. Weiss, "Single molecule dynamics studied by polarization modulation," Phys. Rev. Lett. **77**, 3979 (1996).
128. G. J. Schütz, H. Schindler, and T. Schmidt, "Imaging single-molecule dichroism," Opt. Lett. **22**, 651–653 (1997).
129. M. Prummer, B. Sick, B. Hecht, and U. P. Wild, "Three-dimensional optical polarization tomography of single molecules," J. Chem. Phys. **118**, 9824–9829 (2003).
130. J. N. Forkey, M. E. Quinlan, and Y. E. Goldman, "Measurement of single macromolecule orientation by total internal reflection fluorescence polarization microscopy," Biophys. J. **89**, 1261–1271 (2005).
131. B. P. ölveczky, N. Periasamy, and A. S. Verkman, "Mapping fluorophore distributions in three dimensions by quantitative multiple angle-total internal reflection fluorescence microscopy," Biophys. J. **73**, 2836–2847 (1997).
132. T. Chandler, S. Mehta, H. Shroff, R. Oldenbourg, and P. J. L. Rivière, "Single-fluorophore orientation determination with multiview polarized illumination: modeling and microscope design," Opt. Express **25**, 31309–31325 (2017).
133. D. Pfennig, A. Albrecht, J. Nowak, and P. J. Walla, "A device for exploring the full angular excitation space—can more angular projections improve determination of a molecules 3D-orientation in the presence of noise?" Chem. Phys. **538**, 110853 (2020).
134. H. Ishitobi, I. Nakamura, N. Hayazawa, Z. Sekkat, and S. Kawata, "Orientational imaging of single molecules by using azimuthal and radial polarizations," J. Phys. Chem. B **114**, 2565–2571 (2010).
135. K. D. Weston and L. S. Goldner, "Orientation imaging and reorientation dynamics of single dye molecules," J. Phys. Chem. B **105**, 3453–3462 (2001).
136. K. Adachi, R. Yasuda, H. Noji, H. Itoh, Y. Harada, M. Yoshida, and K. Kinosita, "Stepping rotation of F1-ATPase visualized through angle-resolved single-fluorophore imaging," Proc. Natl. Acad. Sci. USA **97**, 7243–7247 (2000).
137. E. J. Peterman, H. Sosa, L. S. Goldstein, and W. E. Moerner, "Polarized fluorescence microscopy of individual and many kinesin motors bound to axonemal microtubules," Biophys. J. **81**, 2851–2863 (2001).
138. A. B. Asenjo, N. Krohn, and H. Sosa, "Configuration of the two kinesin motor domains during ATP hydrolysis," Nat. Struct. Mol. Biol. **10**, 836–842 (2003).
139. J. N. Forkey, M. E. Quinlan, M. A. Shaw, J. E. T. Corrie, and Y. E. Goldman, "Three-dimensional structural dynamics of myosin V by single-molecule fluorescence polarization," Nature **422**, 399–404 (2003).
140. J. F. Beausang, D. Y. Shroder, P. C. Nelson, and Y. E. Goldman, "Tilting and wobble of myosin V by high-speed single-molecule polarized fluorescence microscopy," Biophys. J. **104**, 1263–1273 (2013).
141. H. Sosa, E. J. Peterman, W. E. Moerner, and L. S. Goldstein, "ADP-induced rocking of the kinesin motor domain revealed by single-molecule fluorescence polarization microscopy," Nat. Struct. Biol. **8**, 540–544 (2001).
142. L. Cognet, G. S. Harms, G. A. Blab, P. H. Lommerse, and T. Schmidt, "Simultaneous dual-color and dual-polarization imaging of single molecules," Appl. Phys. Lett. **77**, 452–454 (2000).
143. A. S. Backer, G. A. King, A. S. Biebricher, J. W. Shepherd, A. Noy, M. C. Leake, I. Heller, G. J. Wuite, and E. J. Peterman, "Elucidating the role of topological constraint on the structure of overstretched DNA

using fluorescence polarization microscopy," J. Phys. Chem. B **125**, 8351–8361 (2021).
144. J. T. Fourkas, "Rapid determination of the three-dimensional orientation of single molecules," Opt. Lett. **26**, 211–213 (2001).
145. L. G. Lippert, T. Dadosh, J. A. Hadden, V. Karnawat, B. T. Diroll, C. B. Murray, E. L. Holzbaur, K. Schulten, S. L. Reck-Peterson, and Y. E. Goldman, "Angular measurements of the dynein ring reveal a stepping mechanism dependent on a flexible stalk," Proc. Natl. Acad. Sci. USA **114**, E4564–E4573 (2017).
146. J. H. Lewis and Z. Lu, "Resolution of Ångström-scale protein conformational changes by analyzing fluorescence anisotropy," Nat. Struct. Mol. Biol. **26**, 802–807 (2019).
147. S. A. Empedocles, R. Neuhauser, and M. G. Bawendi, "Three-dimensional orientation measurements of symmetric single chromophores using polarization microscopy," Nature **399**, 126–130 (1999).
148. C. Lethiec, J. Laverdant, H. Vallon, C. Javaux, B. Dubertret, J. M. Frigerio, C. Schwob, L. Coolen, and A. Maître, "Measurement of three-dimensional dipole orientation of a single fluorescent nanoemitter by emission polarization analysis," Phys. Rev. X **4**, 021037 (2014).
149. J. W. Monaghan, Z. J. O'Dell, S. Sridhar, B. Paranzino, V. Sundaresan, and K. A. Willets, "Calcite-assisted localization and kinetics (clock) microscopy," J. Phys. Chem. Lett. **13**, 10527–10533 (2022).
150. N. C. Vu, Z. Ouzit, C. Lethiec, A. Maître, L. Coolen, F. Lerouge, and J. Laverdant, "Single gold bipyramid nanoparticle orientation measured by plasmon-resonant scattering polarimetry," J. Phys. Chem. Lett. **12**, 752–757 (2021).
151. I. Chung, K. T. Shimizu, and M. G. Bawendi, "Room temperature measurements of the 3D orientation of single CdSe quantum dots using polarization microscopy," Proc. Natl. Acad. Sci. USA **100**, 405–408 (2003).
152. F. Feng, L. T. Nguyen, M. Nasilowski, B. Nadal, B. Dubertret, A. Maître, and L. Coolen, "Probing the fluorescence dipoles of single cubic CdSe/CdS nanoplatelets with vertical or horizontal orientations," ACS Photon. **5**, 1994–1999 (2018).
153. M. Ohmachi, Y. Komori, A. H. Iwane, F. Fujii, T. Jin, and T. Yanagida, "Fluorescence microscopy for simultaneous observation of 3D orientation and movement and its application to quantum rod-tagged myosin V," Proc. Natl. Acad. Sci. USA **109**, 5294–5298 (2012).
154. J. S. Beckwith and H. Yang, "Sub-millisecond translational and orientational dynamics of a freely moving single nanoprobe," J. Phys. Chem. B **125**, 13436–13443 (2021).
155. C. V. Cruz, H. Shaban, A. Kress, N. Bertaux, S. Monneret, M. Mavrakis, J. Savatier, and S. Brasselet, "Quantitative nanoscale imaging of orientational order in biological filaments by polarized superresolution microscopy," Proc. Natl. Acad. Sci. USA **113**, 820–E828 (2016).
156. H. Shaban, C. Valades-Cruz, J. Savatier, and S. Brasselet, "Polarized super-resolution structural imaging inside amyloid fibrils using Thioflavine T," Sci. Rep. **7**, 12482 (2017).
157. S. B. Mehta, M. McQuilken, P. J. L. Riviere, P. Occhipinti, A. Verma, R. Oldenbourg, A. S. Gladfelter, and T. Tani, "Dissection of molecular assembly dynamics by tracking orientation and position of single molecules in live cells," Proc. Natl. Acad. Sci. USA **113**, E6352–E6361 (2016).
158. V. Swaminathan, J. M. Kalappurakkal, S. B. Mehta, P. Nordenfelt, T. I. Moore, N. Koga, D. A. Baker, R. Oldenbourg, T. Tani, S. Mayor, T. A. Springer, and C. M. Waterman, "Actin retrograde flow actively aligns and orients ligand-engaged integrins in focal adhesions," Proc. Natl. Acad. Sci. USA **114**, 10648–10653 (2017).
159. A. K. Adamczyk, T. A. Huijben, M. Sison, A. D. Luca, G. Chiarelli, S. Vanni, S. Brasselet, K. I. Mortensen, F. D. Stefani, M. Pilo-Pais, and G. P. Acuna, "DNA self-assembly of single molecules with deterministic position and orientation," ACS Nano **16**, 16924–16931 (2022).
160. M. Sison, C. A. V. Cruz, C. S. S. Kumar, A. G. Vesga, V. Curcio, L. A. A. Castaneda, M. A. Alonso, M. Mavrakis, and S. Brasselet are preparing a manuscript to be called "4polar3D: single molecule 3D orientation and localization microscopy using a simple pupil diaphragm and ratiometric polarization splitting."
161. E. Bruggeman, O. Zhang, L.-M. Needham, M. Körbel, S. Daly, M. Cheetham, R. Peters, T. Wu, A. S. Klymchenko, S. J. Davis, E. K. Paluch, D. Klenerman, M. D. Lew, K. O'Holleran, and S. F. Lee, "POLCAM: instant molecular orientation microscopy for the life sciences," bioRxiv, 2023.02.07.527479 (2023).
162. K. I. Mortensen, L. S. Churchman, J. A. Spudich, and H. Flyvbjerg, "Optimized localization analysis for single-molecule tracking and super-resolution microscopy," Nat. Methods **7**, 377–381 (2010).
163. K. I. Mortensen, J. Sung, H. Flyvbjerg, and J. A. Spudich, "Optimized measurements of separations and angles between intra-molecular fluorescent markers," Nat. Commun. **6**, 8621 (2015).
164. S. Stallinga and B. Rieger, "Position and orientation estimation of fixed dipole emitters using an effective Hermite point spread function model," Opt. Express **20**, 5896–5921 (2012).
165. T. Ding, T. Wu, H. Mazidi, O. Zhang, and M. D. Lew, "Single-molecule orientation localization microscopy for resolving structural heterogeneities between amyloid fibrils," Optica **7**, 602–607 (2020).
166. R. M. Dickson, D. J. Norris, and W. E. Moerner, "Simultaneous imaging of individual molecules aligned both parallel and perpendicular to the optic axis," Phys. Rev. Lett. **81**, 5322 (1998).
167. M. A. Lieb, L. Novotny, and J. M. Zavislan, "Single-molecule orientations determined by direct emission pattern imaging," J. Opt. Soc. Am. B **21**, 1210–1215 (2004).
168. D. Axelrod, "Fluorescence excitation and imaging of single molecules near dielectric-coated and bare surfaces: a theoretical study," J. Microsc. **247**, 147–160 (2012).
169. A. L. Mattheyses and D. Axelrod, "Fluorescence emission patterns near glass and metal-coated surfaces investigated with back focal plane imaging," J. Biomed. Opt. **10**, 054007 (2005).
170. M. Böhmer and J. Enderlein, "Orientation imaging of single molecules by wide-field epifluorescence microscopy," J. Opt. Soc. Am. B **20**, 554–559 (2003).
171. D. Patra, I. Gregor, and J. Enderlein, "Image analysis of defocused single-molecule images for three-dimensional molecule orientation studies," J. Phys. Chem. A **108**, 6836–6841 (2004).
172. X. Brokmann, M. V. Ehrensperger, J. P. Hermier, A. Triller, and M. Dahan, "Orientational imaging and tracking of single CdSe nanocrystals by defocused microscopy," Chem. Phys. Lett. **406**, 1–3 (2005).
173. R. Schuster, M. Barth, A. Gruber, and F. Cichos, "Defocused wide field fluorescence imaging of single CdSe/ZnS quantum dots," Chem. Phys. Lett. **413**, 280–286 (2005).
174. D. Patra, I. Gregor, J. Enderlein, and M. Sauer, "Defocused imaging of quantum-dot angular distribution of radiation," Appl. Phys. Lett. **87**, 101103 (2005).
175. L. Xiao, Y. Qiao, Y. He, and E. S. Yeung, "Three dimensional orientational imaging of nanoparticles with darkfield microscopy," Anal. Chem. **82**, 5268–5274 (2010).
176. E. Toprak, J. Enderlein, S. Syed, S. A. McKinney, R. G. Petschek, T. Ha, Y. E. Goldman, and P. R. Selvin, "Defocused orientation and position imaging (DOPI) of myosin V," Proc. Natl. Acad. Sci. USA **103**, 6495–6499 (2006).
177. A. Débarre, R. Jaffiol, C. Julien, D. Nutarelli, A. Richard, P. Tchénio, F. Chaput, and J. P. Boilot, "Quantitative determination of the 3D dipole orientation of single molecules," Eur. Phys. J. D **28**, 67–77 (2004).
178. J. Hohlbein and C. G. Hübner, "Simple scheme for rapid three-dimensional orientation determination of the emission dipole of single molecules," Appl. Phys. Lett. **86**, 121104 (2005).
179. J. Hohlbein and C. G. Hübner, "Three-dimensional orientation determination of the emission dipoles of single molecules: the shot-noise limit," J. Chem. Phys. **129**, 94703 (2008).
180. R. Börner, N. Ehrlich, J. Hohlbein, and C. G. Hübner, "Single molecule 3D orientation in time and space: a 6D dynamic study on fluorescently labeled lipid membranes," J. Fluoresc. **26**, 963–975 (2016).
181. H. P. Kao and A. S. Verkman, "Tracking of single fluorescent particles in three dimensions: use of cylindrical optics to encode particle position," Biophys. J. **67**, 1291–1300 (1994).
182. G. Grover, S. Quirin, C. Fiedler, and R. Piestun, "Photon efficient double-helix PSF microscopy with application to 3D photo-activation localization imaging," Biomed. Opt. Express **2**, 3010–3020 (2011).
183. Y. Shechtman, S. J. Sahl, A. S. Backer, and W. E. Moerner, "Optimal point spread function design for 3D imaging," Phys. Rev. Lett. **113**, 133902 (2014).
184. E. R. Dowski and W. T. Cathey, "Extended depth of field through wavefront coding," Appl. Opt. **34**, 1859–1866 (1995).
185. N. K. Efremidis, Z. Chen, M. Segev, and D. N. Christodoulides, "Airy beams and accelerating waves: an overview of recent advances," Optica **6**, 686–701 (2019).

186. W. Chi and N. George, "Electronic imaging using a logarithmic asphere," Opt. Lett. **26**, 875–877 (2001).
187. O. E. Olarte, J. Andilla, E. J. Gualda, and P. Loza-Alvarez, "Light-sheet microscopy: a tutorial," Adv. Opt. Photon. **10**, 111–179 (2018).
188. S. R. P. Pavani and R. Piestun, "Three dimensional tracking of fluorescent microparticles using a photon-limited double-helix response system," Opt. Express **16**, 22048–22057 (2008).
189. Y. Shechtman, L. E. Weiss, A. S. Backer, S. J. Sahl, and W. E. Moerner, "Precise three-dimensional scan-free multiple-particle tracking over large axial ranges with tetrapod point spread functions," Nano Lett. **15**, 4194–4199 (2015).
190. Y. Shechtman, L. E. Weiss, A. S. Backer, M. Y. Lee, and W. E. Moerner, "Multicolour localization microscopy by point-spread-function engineering," Nat. Photonics **10**, 590–595 (2016).
191. G. Grover, S. R. P. Pavani, and R. Piestun, "Performance limits on three-dimensional particle localization in photon-limited microscopy," Opt. Lett. **35**, 3306–3308 (2010).
192. J. Sepiol, J. Jasny, J. Keller, and U. P. Wild, "Single molecules observed by immersion mirror objective. the orientation of terrylene molecules via the direction of its transition dipole moment," Chem. Phys. Lett. **273**, 444–446 (1997).
193. Z. Sikorski and L. M. Davis, "Engineering the collected field for single-molecule orientation determination," Opt. Express **16**, 3660–3673 (2008).
194. M. R. Foreman, P. Török, and C. M. Romero, "Determination of the three-dimensional orientation of single molecules," Opt. Lett. **33**, 1020–1022 (2008).
195. A. S. Backer, M. P. Backlund, M. D. Lew, and W. E. Moerner, "Single-molecule orientation measurements with a quadrated pupil," Opt. Lett. **38**, 1521–1523 (2013).
196. M. Hashimoto, K. Yoshiki, M. Kurihara, N. Hashimoto, and T. Araki, "Orientation detection of a single molecule using pupil filter with electrically controllable polarization pattern," Opt. Rev. **22**, 875–881 (2015).
197. A. Agrawal, S. Quirin, G. Grover, and R. Piestun, "Limits of 3D dipole localization and orientation estimation for single-molecule imaging: towards Green's tensor engineering," Opt. Express **20**, 26667–26680 (2012).
198. A. S. Backer, M. P. Backlund, A. R. V. Diezmann, S. J. Sahl, and W. E. Moerner, "A bisected pupil for studying single-molecule orientational dynamics and its application to three-dimensional super-resolution microscopy," Appl. Phys. Lett. **104**, 193701 (2014).
199. J. Lu, H. Mazidi, T. Ding, O. Zhang, and M. D. Lew, "Single-molecule 3D orientation imaging reveals nanoscale compositional heterogeneity in lipid membranes," Angew. Chem. (Int. Ed.) **59**, 17572–17579 (2020).
200. C. N. Hulleman, R. O. Thorsen, E. Kim, C. Dekker, S. Stallinga, and B. Rieger, "Simultaneous orientation and 3D localization microscopy with a vortex point spread function," Nat. Commun. **12**, 5934 (2021).
201. T. Ding and M. D. Lew, "Single-molecule localization microscopy of 3D orientation and anisotropic wobble using a polarized vortex point spread function," J. Phys. Chem. B **125**, 12718–12729 (2021).
202. T. Wu, J. Lu, and M. D. Lew, "Dipole-spread-function engineering for simultaneously measuring the 3D orientations and 3D positions of fluorescent molecules," Optica **9**, 505–511 (2022).
203. O. Zhang, Z. Guo, Y. He, T. Wu, M. D. Vahey, and M. D. Lew, "Six-dimensional single-molecule imaging with isotropic resolution using a multi-view reflector microscope," Nat. Photonics **17**, 179–186 (2023).
204. O. Zhang, W. Zhou, J. Lu, T. Wu, and M. D. Lew, "Resolving the three-dimensional rotational and translational dynamics of single molecules using radially and azimuthally polarized fluorescence," Nano Lett. **22**, 1024–1031 (2022).
205. A. Aristov, B. Lelandais, E. Rensen, and C. Zimmer, "ZOLA-3D allows flexible 3D localization microscopy over an adjustable axial range," Nat. Commun. **9**, 2409 (2018).
206. N. A. Rubin, Z. Shi, and F. Capasso, "Polarization in diffractive optics and metasurfaces," Adv. Opt. Photon. **13**, 836–970 (2021).
207. P. Réfrégier, *Noise Theory and Application to Physics: From Fluctuations to Information* (Springer, 2003).
208. P. Jouchet, A. R. Roy, and W. E. Moerner, "Combining deep learning approaches and point spread function engineering for simultaneous 3D position and 3D orientation measurements of fluorescent single molecules," Opt. Commun. **542**, 129589 (2023).
209. O. Zhang and M. D. Lew, "Single-molecule orientation localization microscopy I: fundamental limits," J. Opt. Soc. Am. A **36**, 277–287 (2021).
210. O. Zhang and M. D. Lew, "Single-molecule orientation localization microscopy II: a performance comparison," J. Opt. Soc. Am. A **38**, 288–297 (2021).
211. A. Vella and M. A. Alonso, "Optimal birefringence distributions for imaging polarimetry," Opt. Express **27**, 36799–36814 (2019).
212. R. Luchowski, Z. Gryczynski, Z. Földes-Papp, A. Chang, J. Borejdo, P. Sarkar, and I. Gryczynski, "Polarized fluorescent nanospheres," Opt. Express **18**, 4289–4299 (2010).
213. L. Neumann, J. van 't Oever, and N. F. van Hulst, "A resonant scanning dipole-antenna probe for enhanced nanoscale imaging," Nano Lett. **13**, 5070–5074 (2013).
214. P. N. Petrov, Y. Shechtman, and W. E. Moerner, "Measurement-based estimation of global pupil functions in 3D localization microscopy," Opt. Express **25**, 7945–7959 (2017).
215. Y. Li, Y.-L. Wu, P. Hoess, M. Mund, and J. Ries, "Depth-dependent PSF calibration and aberration correction for 3D single-molecule localization," Biomed. Opt. Express **10**, 2708–2718 (2019).
216. T. Yan, C. J. Richardson, M. Zhang, and A. Gahlmann, "Computational correction of spatially variant optical aberrations in 3D single-molecule localization microscopy," Opt. Express **27**, 12582–12599 (2019).
217. L. A. Alemán-Castañeda, S. Y.-T. Feng, R. Gutiérrez-Cuevas, I. Herrera, T. G. Brown, S. Brasselet, and M. A. Alonso, "Using fluorescent beads to emulate single fluorophores," J. Opt. Soc. Am. A **39**, C167–C178 (2022).
218. D. Sage, T.-A. Pham, H. Babcock, *et al.*, "Super-resolution fight club: assessment of 2D and 3D single-molecule localization microscopy software," Nat. Methods **16**, 387–395 (2019).
219. R. Gutiérrez-Cuevas, L. Alemán-Castañeda, I. Herrera, S. Brasselet, and M. Alonso, "Characterization of polarization dependence in super-resolution fluorescent microscopy via phase retrieval," arXiv, arXiv:2309.03611 (2023).
220. A. Vella and M. A. Alonso, "Maximum likelihood estimation in the context of an optical measurement," Prog. Opt. **65**, 231–311 (2020).
221. R. J. Ober, S. Ram, and E. S. Ward, "Localization accuracy in single-molecule microscopy," Biophys. J. **86**, 1185–1200 (2004).
222. S. Quirin, S. R. P. Pavani, and R. Piestun, "Optimal 3D single-molecule localization for superresolution microscopy with aberrations and engineered point spread functions," Proc. Natl. Acad. Sci. USA **109**, 675–679 (2012).
223. E. Nehme, L. E. Weiss, T. Michaeli, and Y. Shechtman, "Deep-STORM: super-resolution single-molecule microscopy by deep learning," Optica **5**, 458–464 (2018).
224. L. Möckl, A. R. Roy, and W. E. Moerner, "Deep learning in single-molecule microscopy: fundamentals, caveats, and recent developments [invited]," Biomed. Opt. Express **11**, 1633–1661 (2020).
225. P. Zhang, S. Liu, A. Chaurasia, D. Ma, M. J. Mlodzianoski, E. Culurciello, and F. Huang, "Analyzing complex single-molecule emission patterns with deep learning," Nat. Methods **15**, 913–916 (2018).
226. T. Wu, P. Lu, M. A. Rahman, M. A. Rahman, X. Li, and M. D. Lew, "Deep-SMOLM: deep learning resolves the 3D orientations and 2D positions of overlapping single molecules with optimal nanoscale resolution," Opt. Express **30**, 36761–36773 (2022).
227. J. Schaffer, A. Volkmer, C. Eggeling, V. Subramaniam, G. Striker, and C. A. Seidel, "Identification of single molecules in aqueous solution by time-resolved fluorescence anisotropy," J. Phys. Chem. A **103**, 331–336 (1998).
228. K. Lindfors, A. Priimagi, T. Setälä, A. Shevchenko, A. T. Friberg, and M. Kaivola, "Local polarization of tightly focused unpolarized light," Nat. Photonics **1**, 228–231 (2007).
229. T. Bauer, P. Banzer, E. Karimi, S. Orlov, A. Rubano, L. Marrucci, E. Santamato, R. W. Boyd, and G. Leuchs, "Observation of optical polarization Möbius strips," Science **347**, 964–966 (2015).
230. J. Eismann, L. Nicholls, D. Roth, M. Alonso, P. Banzer, F. Rodríguez-Fortuño, A. Zayats, F. Nori, and K. Bliokh, "Transverse spinning of unpolarized light," Nat. Photonics **15**, 156–161 (2021).